

Dissertation presented to the Instituto Tecnológico de Aeronáutica, in partial fulfillment of the requirements for the Degree of Master in Science in the Graduate Program of Space Science and Technology, Field of Space Systems, Testing and Launching.

Renan Santos

**HIGH-ORDER CONSERVATIVE INTERPOLATION ON
OVERSET MESHES FOR UNSTEADY AERODYNAMICS
APPLICATIONS**

Dissertation approved in its final version by signatories below:



Prof. Dr. João Luiz Filgueiras de Azevedo

Advisor

Prof. Dr. Emília Villani
Pro-Rector of Graduate Courses

Campo Montenegro
São José dos Campos, SP - Brazil
2022

Cataloging-in Publication Data
Documentation and Information Division

Santos, Renan

High-Order Conservative Interpolation on Overset Meshes for Unsteady Aerodynamics Applications /
Renan Santos.

São José dos Campos, 2022.

101f.

Dissertation of Master in Science – Program of Space Science and Technology. Field of Space Systems,
Testing and Launching – Aeronautics Institute of Technology, 2022. Advisor: Prof. Dr. João Luiz
Filgueiras de Azevedo.

1. Computational Fluid Dynamics. 2. Unsteady Aerodynamics. 3. High-Order Methods. 4. Overset Grid.
I. Instituto Tecnológico de Aeronáutica. II. High-Order Conservative Interpolation on Overset Meshes for
Unsteady Aerodynamics Applications.

BIBLIOGRAPHIC REFERENCE

SANTOS, Renan. **High-Order Conservative Interpolation on Overset Meshes for Unsteady Aerodynamics Applications**. 2022. 101f. Dissertation of Master in Science in Space Systems, Testing and Launching – Instituto Tecnológico de Aeronáutica, São José dos Campos.

CESSION OF RIGHTS

AUTHOR'S NAME: Renan Santos

PUBLICATION TITLE: High-Order Conservative Interpolation on Overset Meshes for Unsteady Aerodynamics Applications.

PUBLICATION KIND/YEAR: Dissertation / 2022

It is granted to Aeronautics Institute of Technology permission to reproduce copies of this dissertation to only loan or to sell copies for academic and scientific purposes. The author reserves other publication rights and no part of this dissertation can be reproduced without the authorization of the author.



Renan Santos
Av. Universitário, 585
06.542-089 – Santana de Parnaíba–SP

HIGH-ORDER CONSERVATIVE INTERPOLATION ON OVERSET MESHES FOR UNSTEADY AERODYNAMICS APPLICATIONS

Renan Santos

Thesis Committee Composition:

Prof. Dr.	Maria Luísa Collucci da Costa Reis	Chairperson	-	ITA
Prof. Dr.	João Luiz Filgueiras de Azevedo	Advisor	-	ITA
Prof. Dr.	Cayo Prado Fernandes Francisco	Internal Member	-	ITA
Prof. Dr.	Paulo Roberto Maciel Lyra	External Member	-	UFPE

ITA

À minha família,
pais, padrasto e esposa.

Acknowledgments

Antes de tudo, eu gostaria de profundamente agradecer à minha mãe, Antonia, por todo amor, confiança e ensinamentos que me proveu. É graças ao seu incondicional amor e esforço que pude chegar aqui. Ao seu lado, gostaria também de agradecer por todo o suporte e carinho do meu padrasto, José Eraldo, que sempre me ajudou em tudo o que eu precisei. Em especial, eu gostaria de agradecer a toda força, paciência e incentivo que minha amada esposa, Ana Paula, tem me dado durante todo esse tempo. Tenho um extremo orgulho da nossa história que sem sombra de dúvidas me fez e ainda me faz uma pessoa melhor.

Gostaria de agradecer ao meu orientador, Professor Azevedo, não somente pelo massivo conhecimento que possui, mas primordialmente pela sua ética e profissionalismo. Acredito que de todas as oportunidades que tive dentre conversas e aulas, não houve uma única vez em que não saí carregado de ânimo a aprender e extremamente motivado. Próximo ao Lab, gostaria de especialmente agradecer ao Fábio Mallaco, Pepê, Leo e Marco por toda ajuda e ensinamentos.

Um pouco mais longe do ITA, gostaria de agradecer aos meus amigos de vida: André, Sabiá e Daniel Thoma. Sem eles o tempo de ensino médio, faculdade, e mestrado, não teria sido tão empolgante e divertido. Em particular, gostaria de agradecer o André pelas diversas conversas técnicas que trocamos, por todas as vezes que me ajudou a entender melhor sobre um problema

e por toda a proximidade que temos até hoje. Muito obrigado por tudo, amigos.

Gostaria de declarar meus sinceros agradecimentos à minha segunda família: Willians, Valquíria, Fernando, Amanda, inclusive o Guilherme. Por pelo menos metade da minha vida, essas pessoas têm me proporcionado grandiosíssimos momentos de felicidade e memoráveis confraternizações. Por fim, ao Marquinhos que será cena de um futuro capítulo.

*“The first principle is that you must not fool yourself
and you are the easiest person to fool.”*

— RICHARD P. FEYNMAN

Resumo

A capacidade de lidar com escoamentos não-estacionários sob geometrias complexas de forma eficiente e com alta ordem de acurácia é frequentemente bastante desejável pela indústria aeroespacial. Pesquisas recentes no contexto de malhas sobrepostas, que promovem alta ordem no processo de reconstrução dos termos de fluxo das equações da mecânica dos fluidos, têm apresentado ótimos resultados para aplicações que incluem corpos móveis sem a necessidade de novas gerações de malha. A habilidade de propostas que acoplam tais requisitos é de extrema importância, por exemplo, ao se considerar escoamentos que envolvam asas rotativas ou problemas similares. No presente trabalho, um método numérico de alta ordem de precisão no processo de reconstrução dos termos de fluxo é implementado e adaptado para considerar técnicas de interpolação conservativa de alta ordem com uma estrutura de dados sobre os nós da malha via o algoritmo kd-tree para efetuar a comunicação de informação entre malhas sobrepostas. O escoamento é modelado pelas equações de Euler em 2-D discretizadas no espaço pelo método das Diferenças Espectrais (SD) e um método explícito de integração temporal via um método SSP Runge-Kutta. Em cenários de malhas sobrepostas, duas malhas não estruturadas são geradas: uma malha de fundo incluindo todo o domínio do fluido e uma malha próxima ao corpo de interesse. A fim de determinar qual célula da malha dadora envolve um nó específico

da malha receptora, ambas as malhas são representadas por uma estrutura de dados em árvore de seus nós, a qual provê uma complexidade temporal logarítmica de ordem $O(k \log N)$ para o processo de busca geométrica, onde k é o número de pontos de fluxo alocados ao longo do contorno externo da malha receptora e N é o número de nós da malha doadora. Além disso, a solução é interpolada das células doadoras para os pontos na malha receptora através da expansão polinomial pelos pontos de solução da célula doadora e, em seguida, impõe-se como condição de contorno fraca para reconstruir o fluxo de forma exata via um esquema de solução aproximada do problema de Riemann tal qual é feito em outras faces entre células. A implementação é avaliada em diferentes testes de validação extraídos do evento internacional de métodos de alta ordem em CFD - 5th International Workshop on High-Order CFD Methods (HiOCFD5). Por fim, estudos da acurácia e convergência são realizados para ambos os casos de malha única e malhas sobrepostas comparando-se os resultados com a literatura.

Abstract

The capability of handling unsteady flows over complex geometries with efficiency and high-order accuracy is quite often desirable for the aerospace industry. Recent research on high-order overset flux reconstruction methods have shown successful results over moving boundary problems without the need of remeshing. The ability of accurately handling such type of requirements is very important, for instance, when addressing rotary wing flows and similar problems.

In the present study, a high-order flux reconstruction solver is implemented coupled with a high-order conservative interpolation approach and a kd-tree algorithm over the mesh nodes for data communication in the overset regions. The flow is modeled by the 2-D Euler equations discretized in space with a Spectral Differences method and an explicit strong stability-preserving Runge-Kutta scheme for time integration. In the overset grid scenarios, two unstructured grids are generated: a background mesh including all the fluid box domain and a near-body mesh. In order to determine which cell of the donor grid embeds a specific node in the receiver grid, both mesh nodes are implemented with a tree data structure expecting the logarithmic time complexity of $O(k \cdot \log N)$ in the geometric search, where k is the number of flux points over the boundary interfaces of the receiver mesh and N the number of nodes in the donor grid. Furthermore, the solution is interpolated from the donor cell to the receiver grid point based on the donor cell

polynomial expansion at the solution points and, then, imposed in a weak manner as a boundary condition to exactly reconstruct the flux with the approximate Riemann solver, as for any other interior face. The implementation is tested for different validation problems from the 5th International Workshop on High-Order CFD Methods (HiOCFD5). Additionally, accuracy and convergence studies are performed on both single and overset grid approaches and compared to results in the literature.

Contents

LIST OF FIGURES	xvii
LIST OF TABLES	xxi
LIST OF ABBREVIATIONS AND ACRONYMS	xxii
LIST OF SYMBOLS	xxiii
1 INTRODUCTION	26
1.1 Motivation of the Present Work	26
1.2 Objective	28
1.3 Dissertation Outline	29
2 PHYSICAL FORMULATION	30
2.1 Conservation Laws	30

2.2 Euler Equations	31
2.3 Formulation of Characteristic Equations	33
2.4 Boundary Conditions	35
2.4.1 Slip Wall	35
2.4.2 Inlet	36
2.4.3 Outlet	37
2.4.4 Non-Reflective Farfield	38
2.5 Non-Dimensionalization	38
3 NUMERICAL FORMULATION	40
3.1 Spectral Difference Method	40
3.1.1 Discretization	41
3.1.2 Space Transformation	42
3.1.3 Base Polynomials	42
3.2 Riemann Solver	43
3.3 Time Integration	48
3.4 Evaluation Metrics	50
3.4.1 Residue	50
3.4.2 Isentropic Flows	50
3.4.3 Analytical Solution Error	51

4 CONSERVATIVE HIGH-ORDER INTERPOLATION	52
4.1 Overset Grids	52
4.2 Overset Assembly	53
4.2.1 Geometric Search	53
4.2.2 Receptor-Donor Connectivity	57
4.2.3 Extension to Curved Meshes	59
4.2.4 Hole-Cutting	61
4.3 Data Communication	62
4.3.1 Data Interpolation	62
4.3.2 Standard Space Projection	64
5 RESULTS	68
5.1 Ringleb Flow	68
5.2 Inviscid Cylinder	75
5.3 Isentropic Vortex	83
6 CONCLUSION	94
6.1 Concluding Remarks	94
6.2 Future Work	96

BIBLIOGRAPHY	101
--------------------	-----

List of Figures

FIGURE 2.1 – Boundary condition for one-dimensional inlet for Euler Equations with the internal (gray) and external (dark gray) physical regions of dependency [1].	36
FIGURE 2.2 – Boundary condition for one-dimensional outlet for Euler Equations with the internal (gray) and external (dark gray) physical regions of dependency [1].	37
FIGURE 3.1 – Quadrilateral in computational space for 2nd-order Spectral Differences, $p = 1$	43
FIGURE 4.1 – Overset meshes setup: background mesh in black and near-body mesh in orange.	53
FIGURE 4.2 – Overset grid setup and cell type definitions for a illustrative cylinder example.	54
FIGURE 4.3 – kD-tree geometrical view for a given set of points.	55
FIGURE 4.4 – kD-tree radius test.	57

FIGURE 4.5 – Donor cell searching procedure given the target node (red triangle) and the nearest donor node (blue circle). The failed test is done over the left bottom cell and the successful test over the right bottom cell.	58
FIGURE 4.6 – Inward facing edges (in yellow) of the fringe cell circuit in the background mesh.	59
FIGURE 4.7 – Cell searching procedure issue for curved cells.	60
FIGURE 4.8 – High-order edges nodes inclusion in the cell searching procedure.	61
FIGURE 4.9 – Hole-cutting flag (blue) propagation using a Breadth-First Search (BFS) algorithm conditioned by the fringe cell circuit (red).	62
FIGURE 4.10 – Data communication nodes setup at the overset region for face-based and element-based approaches.	63
FIGURE 4.11 – The target node is projected from the receiver to the donor computational space.	64
FIGURE 4.12 – The solution is interpolated to the target coordinate inside the donor computational space.	65
FIGURE 4.13 – The interpolated solution (arrow) is then projected back to the receiver computational space.	66
FIGURE 4.14 – Imposition of the interpolated solution as a weak boundary condition using flux reconstruction.	67
FIGURE 5.1 – Ringleb flow boundary conditions (left) and initial mesh (right).	70

FIGURE 5.2 – Meshes for the Ringleb flow test case for different P values.	71
FIGURE 5.3 – Analytical Ringleb flow solution: Mach number contours.	72
FIGURE 5.4 – L2-norm of the density residue for the Ringleb flow for different values of P for the same mesh (Q4).	73
FIGURE 5.5 – Converged numerical Mach number contour solution for the Ringleb flow test case for different P values.	74
FIGURE 5.6 – Inviscid cylinder boundary conditions sketch for single mesh (left) and overset mesh (right) cases.	76
FIGURE 5.7 – Cylinder single and overset meshes with 1:100 cylinder radius ratio. .	77
FIGURE 5.8 – Close-up views of the cylinder single and overset Spectral Difference meshes for two different scenarios of mesh and solver orders: P2Q1 and P5Q4.	78
FIGURE 5.9 – Cylinder overset grid special cells for the background (left) and near-body meshes (right). Fringes in light-gray, holes in red, and fluid cells in blue.	79
FIGURE 5.10 – Comparison of the L2-norm of the density residue for the single and overset cases with different mesh and solver orders.	80
FIGURE 5.11 – Cylinder single and overset grid solution in terms of Mach number contours for P2Q1.	81
FIGURE 5.12 – Cylinder single and overset grid solution in terms of Mach number contours for P5Q4.	83

FIGURE 5.13 – Spectral Difference mesh for the 32×32 background and 10×10 near-body mesh case.	86
FIGURE 5.14 – Initial solution for the density in the overset setup.	87
FIGURE 5.15 – Fringe and hole cells for different orders of accuracy of the Spectral Difference method in the overset vortex case.	88
FIGURE 5.16 – Special case when a flux-point of a fringe cell is out of the near-body mesh (green dots). Background fringe cells in light blue, hole cells in light orange and the special case of fringe cells in red.	89
FIGURE 5.17 – Numerical density contours for the solution of the vortex overset case with $P=4$ after different time periods.	91
FIGURE 5.18 – Comparison of the L2-norm of the entropy error for the single and overset cases with different values for P and mesh size.	92

List of Tables

TABLE 5.1 – Values of the median CPU time per iteration in milliseconds.	92
--	----

List of Abbreviations and Acronyms

1D	One Dimensional
2D	Two Dimensional
BFS	Breadth-First-Search
CFD	Computational Fluid Dynamics
CFL	Courant-Friedrichs-Lowy
CPR	Correction Procedure via Reconstruction
FP	Flux Points
FR	Flux Reconstruction
HiOCFD	High-Order Computational Fluid Dynamics Workshop
NASA	National Aeronautics and Space Administration
RK	Runge-Kutta
SD	Spectral Differences
SP	Solution Points
SSP	Strongly-Stability Preserving

List of Symbols

Latin Characters

A	Flux transformation matrix
c	Speed of sound
c_p	Heat capacity at constant pressure
c_v	Heat capacity at constant volume
e	Internal energy
\tilde{e}	Roe-averaged kinetic energy
E	Total energy
F	Vector of inviscid flux in x-direction
G	Vector of inviscid flux in y-direction
h	Specific enthalpy
\tilde{h}	Roe-averaged enthalpy
H	Enthalpy
I	Identity matrix

J	Jacobian matrix of the standard space transformation
$ J $	Jacobian matrix determinant
$\hat{\mathbf{k}}$	Wave propagating direction
L	Characteristic length scale
L_m	Lagrange m-th polynomial basis
\mathbf{n}	Vector for the normal wall direction
N_p	Number of basis functions
p	Static pressure
\tilde{p}	Roe-averaged pressure
\mathbf{Q}	Vector of conservative variables
R	Universal gas constant
t	Time
T	Temperature
u	Velocity in x-direction
\tilde{u}	Roe-averaged x-direction velocity
\mathbf{U}	Vector of fluid velocities
v	Velocity in y-direction
\tilde{v}	Roe-averaged y-direction velocity
x, y, z	Cartesian spatial coordinates
\mathbf{W}	Vector of characteristic variables

Greek Characters

Λ	Eigenvector matrix for the characteristic waves
∇	Nabla operator
$\tilde{\alpha}$	Roe wave strength
γ	Isentropic coefficient
$\tilde{\lambda}$	Roe eigenvalues
ρ	Density
$\tilde{\rho}$	Roe-averaged density
ξ, η	Standard space coordinates

Superscripts

$\overline{()$	Non-dimensionalized property
$\tilde{()$	Computational space property

Subscripts

$(\cdot)_{ref}$	Reference property
$(\cdot)_\infty$	Free-stream property
$(\cdot)_s$	At constant entropy
$(\cdot)_L$	Left hand side property of an interface
$(\cdot)_R$	Right hand side property of an interface

1 Introduction

1.1 Motivation of the Present Work

Several applications in the aerospace context require efficient, accurate, and robust simulations including complex geometries with moving bodies. For instance, the simulations addressing the flow over the blades of a rotorcraft, the drop of a cargo, or even the movement of control surfaces in a maneuver can be quite challenging due to the moving boundary interaction with a vortex dominated flow [2, 3, 4]. The misrepresentation of these complex fluid structure interactions can affect multidisciplinary topics of an aerospace project. Eventually, when a vortex comes out of the tip of a blade, this vortex may travel up to important structures like the control surfaces and, then, may jeopardize some key engineering specifications of a project. Therefore, the consideration of movable structures with high accuracy and possibly long-time simulation turns out to be very desirable in these contexts.

In general, most of the Computational Fluid Dynamics simulations setup a unique mesh to represent the fluid-emerged body geometry altogether with a discrete specialized sample of the continuous physical domain into the computer. However, in scenarios with moving bodies, despite the existence of different methodologies to adapt the mesh given the body's move-

ment [5, 6], it can present a high computational cost during the simulation. Most commonly, a remeshing step is applied to the entire mesh domain everytime the deformed mesh reaches a low quality. In this sense, the treatment for moving boundaries uniquely described by single mesh is too cumbersome. On the other hand, research on overlapped multiple meshes has been addressed to overcome this limitation aiming to provide flexibility in the geometric representation, boundary movement and deformation, and high-order accuracy at a suitable cost [7, 8, 9, 10]. Commonly named as overset grids or Chimera mesh, the domain representation is setup by two mesh categories: a background mesh and a near-body mesh. The background mesh contains the overall simulation domain, while the near-body mesh moves with a fluid emerged body or fluid structure of interest such as a vortex. Thus, in the overset grid setup, only the near-body mesh needs to be adapted given a body boundary deformation or movement leaving a major part of the fluid domain in the background mesh as strictly static.

In order to provide an overset grid solver, some additional procedures are often necessary to couple the solution data from one mesh to the other. At the preprocessing stage, a connectivity relationship needs to be established so that the cells at the external boundary of the near-body mesh can identify donors cells from the background. Furthermore, some background mesh cells are fully-overlapped by the near-body mesh and then no solver iteration is needed, once the simulation can be provided by the near-body mesh cells in these areas. The background donor cells will then interface skipped cells where the solution is not provided and, in a similar manner, the receptor-donor relationship is defined to gather data from the near-body mesh. Moreover, the data communication is done at each time integration step and applied as weak boundary condition at the overset region.

Nonetheless, previous benchmark overset grid solvers only considered 2nd order resolution for the near-body mesh and linear interpolations for the data communication procedure [11, 12]. With a low-order solver, not only the physical representation can be affected through a low resolution of phenomena such as vortex wakes and strong discontinuities, but also the computational cost is higher given a target order of accuracy which can be cumbersome and only achievable over mesh refinement. On the other hand, recent spatial discretization methods have been proposed providing arbitrary efficiency, robustness and accuracy in the high-order community [13, 14, 15, 16, 17].

In the recent decade, a high-order method framework, named as FR/CPR for Flux Reconstruction/Correction Procedure via Reconstruction, has presented state-of-the-art solutions for several benchmark validation tests, in a broad and efficient manner, consolidating several high-order methods in a concise formulation [18]. Due to the aforementioned complexities to provide a proper accurate and efficient solution on unsteady aerodynamics applications, a high-order method becomes important and a suitable candidate for the present work. Additionally, high-order meshes, which better represent complex geometries due to curvature representation from its curved cells, have been reported to indeed impact in the achievement of the high-order method accuracy [19] and, therefore, they are also relevant for this project.

1.2 Objective

The present work aims to study approaches to achieve a high-order accurate and conservative interpolation between unstructured overset grids. The order of accuracy of the implementation is investigated using the common high-order benchmark test cases for both single and

overset grid simulations. Since low-order meshes can limit the accuracy of a high-order method by producing non-physical oscillations over unsuitable geometrical boundary representations, curved meshes are also considered for the present high-order solver. Finally, the work discusses about some challenges in the overset region communication when considering curved cells.

1.3 Dissertation Outline

The sections of this dissertation to address the topics of the present work are organized as follows. Section 2 describes the physical formulation used throughout the project. Section 3 reviews the numerical method based on a high-order polynomial representation coupled with high-order meshes. Section 4 contains a detailed discussion for the overset grid methodology including the geometric search procedure and conservative high-order interpolation. Section 5 presents the results comparing single and overset grid and high-order accuracy test cases. Finally, concluding remarks and future work extensions for the present project are discussed in Section 6.

2 Physical Formulation

2.1 Conservation Laws

The Conservation Laws are the fundamental physical principles that describe the nature's observable behavior of mass continuity, momentum and energy conservation. Given a finite volume in space assumed as a continuum domain where only macroscopic properties are sufficient to describe its behavior, the conservation laws formulate that the total variation of a conservative quantity in a unit time is equivalent of the total amount of this quantity that flows across the volume's surfaces plus any external source. This principle can be written in differential form as

$$\frac{\partial \mathbf{Q}}{\partial t} = -\nabla \cdot \mathbf{F} + \mathbf{S}. \quad (2.1)$$

where \mathbf{Q} represents the fluid macroscopic quantities such as mass, momentum and total energy per unit of volume, and \mathbf{F} the flux of these quantities that passes across the volume's surfaces, and \mathbf{S} the source or sink term per unit of volume.

2.2 Euler Equations

The Euler equations are the mathematical formulation that model compressible, non-heat-conducting, inviscid flows composed by the conservation laws of mass, momentum and total energy. The physical phenomena represented by the Euler equations are, hence, fluid flows on the edge of almost zero viscosity where the convective effects are dominant. These equations can be expressed in several forms, nevertheless, in the presence of physical discontinuities such as contact and shock waves, it is recommended the use of the conservation form to correctly compute the intensity and propagation speed of these waves [1]. The system of the 2-D Euler equations in the conservative form, in the absence of source terms, can be written as

$$\frac{\partial \mathbf{Q}}{\partial t} + \frac{\partial \mathbf{F}}{\partial x} + \frac{\partial \mathbf{G}}{\partial y} = 0 . \quad (2.2)$$

where \mathbf{Q} is the vector of conserved variables, \mathbf{F} and \mathbf{G} the inviscid flux vectors for x and y directions, given by

$$\mathbf{Q} = \begin{Bmatrix} \rho \\ \rho u \\ \rho v \\ E \end{Bmatrix} , \quad \mathbf{F} = \begin{Bmatrix} \rho u \\ \rho u^2 + p \\ \rho u v \\ u(E + p) \end{Bmatrix} , \quad \mathbf{G} = \begin{Bmatrix} \rho v \\ \rho u v \\ \rho v^2 + p \\ v(E + p) \end{Bmatrix} . \quad (2.3)$$

forming a hyperbolic system of first-order partial differential equations. The ρ is the density, p is the pressure, E is the total energy, u and v the velocity components in x and y directions, respectively, representing the set of primitive variables. In order to form a closed system of equations,

an additional relation between the pressure and the other primitive variables is defined from the equation of state for perfect gases as

$$p = (\gamma - 1) \left[E - \frac{1}{2} \rho(u^2 + v^2) \right] \quad (2.4)$$

where γ is the isentropic exponent. Equation (2.4) can be derived by the assumption of negligible intermolecular forces in the ideal gas law, $p = \rho RT$, where T is the fluid temperature and R the specific gas constant. The assumptions behind the ideal gas law are only valid when the gas particles have negligible volume, have perfect elastic collisions with no energy loss, particles are equally sized and no intermolecular forces are presented. Additionally, the fluid is also assumed to be thermally and calorically perfect, i.e., the fluid internal energy, e , and enthalpy, H , are only functions of the temperature and the specific heat capacity at constant volume, c_v , and pressure, c_p , are constants. Specific enthalpy, h , and internal energy per unit of mass can then be obtained from

$$e = c_v T \quad h = \frac{H}{\rho} = c_p T$$

By the definition of enthalpy

$$h = e + \frac{p}{\rho} \quad (2.5)$$

and Eq. (2.4), a relation between the specific heat capacity can be obtained

$$c_p - c_v = R \quad (2.6)$$

which can be solved for each specific heat capacity coefficients by defining the ratio of specific heat capacities as

$$\gamma = \frac{c_p}{c_v} \quad (2.7)$$

leading to the expressions

$$c_p = \frac{\gamma R}{\gamma - 1} \quad c_v = \frac{R}{\gamma - 1} \quad (2.8)$$

2.3 Formulation of Characteristic Equations

The flux vector of the Euler equations can be rewritten as a function of the fluid conservative properties from the \mathbf{Q} vector components

$$\mathbf{Q} = \begin{Bmatrix} \rho \\ \rho u \\ \rho v \\ E \end{Bmatrix} = \begin{Bmatrix} q_1 \\ q_2 \\ q_3 \\ q_4 \end{Bmatrix} \quad (2.9)$$

so that the flux vectors become

$$\mathbf{F} = \begin{Bmatrix} q_2 \\ \frac{q_2^2}{q_1} + p \\ \frac{q_2 q_3}{q_1} \\ \frac{q_2}{q_1} (q_4 + p) \end{Bmatrix} \quad \mathbf{G} = \begin{Bmatrix} q_3 \\ \frac{q_3}{q_1} q_2 \\ \frac{q_3^2}{q_1} + p \\ \frac{q_3}{q_1} (q_4 + p) \end{Bmatrix} \quad (2.10)$$

where the pressure p can also be represented by the \mathbf{Q} components as

$$p = (\gamma - 1) \left[q_4 - \frac{(q_2^2 + q_3^2)}{2q_1} \right] \quad (2.11)$$

This transformation of the flux allows to represent the Euler equations as a convection equation of the fluid properties \mathbf{Q} so that

$$\frac{\partial \mathbf{Q}}{\partial t} + [\mathbf{A}(Q) \cdot \nabla] \mathbf{Q} = 0 \quad (2.12)$$

where the Jacobian matrix of the flux transformation \mathbf{A} is defined as

$$\mathbf{A} := \frac{\partial \mathbf{F}}{\partial Q} = \frac{1}{u^2 - c^2} \begin{bmatrix} 0 & 1 & 0 & 0 \\ (\gamma - 1)\frac{q}{2} - u^2 & (3 - \gamma)u & (1 - \gamma)v & \gamma - 1 \\ -uv & v & u & 0 \\ \left(\frac{\gamma-1}{2}q^2 - h\right)u & h + (1 - \gamma)u^2 & (1 - \gamma)uv & \gamma u \end{bmatrix} \quad (2.13)$$

where $q = u^2 + v^2$ is the squared velocity magnitude.

This reinforces that the physical behavior of the fluid properties described by Euler equations are indeed dominated by a wave-like phenomena. Moreover, the Jacobian matrix \mathbf{A} can be diagonalized by solving

$$\det|\lambda \mathbf{I} - \mathbf{A} \cdot \hat{\mathbf{k}}| = 0 \quad (2.14)$$

which can be used to decouple the Euler equations onto its characteristic formulation in a wave

propagating direction $\hat{\mathbf{k}}$ as

$$\frac{\partial \mathbf{W}}{\partial t} + \Lambda \frac{\partial \mathbf{W}}{\partial x_k} = 0 \quad (2.15)$$

where \mathbf{W} is the vector of characteristic variables and Λ is the diagonal eigenvalue matrix which at the k direction is defined as

$$\Lambda := \begin{bmatrix} u_k & 0 & 0 & 0 \\ 0 & u_k & 0 & 0 \\ 0 & 0 & (u_k + c) & 0 \\ 0 & 0 & 0 & (u_k - c) \end{bmatrix} \quad (2.16)$$

where $u_k := \mathbf{U} \cdot \hat{\mathbf{k}}$, with \mathbf{U} as the vector of fluid velocities.

2.4 Boundary Conditions

2.4.1 Slip Wall

In the absence of viscosity and heat conduction, the physical behavior expected at an impenetrable wall is purely reflection, i.e., the fluid velocity at an object surface is zero in the normal direction and only the tangential velocity component is unchanged. Hence, the name slip wall boundary condition, in which the fluid is assumed to slip around the surfaces and no boundary layer is formed. Mathematically, the local velocity vector at the wall can then be written as

$$\mathbf{U}_n = (\mathbf{U} \cdot \mathbf{n}) = 0 \quad (2.17)$$

2.4.2 Inlet

At an inlet boundary where the fluid is moving towards the inside of the domain different conditions have to be considered depending on the velocity that the information is transported with respect to the local speed of sound c , i.e., whether it is a supersonic or subsonic inlet. Equation (2.15) states that the Euler equations are associated with the propagation of three types of waves with velocities $u - c$, u and $u + c$ in a simplified one-dimensional x -direction.

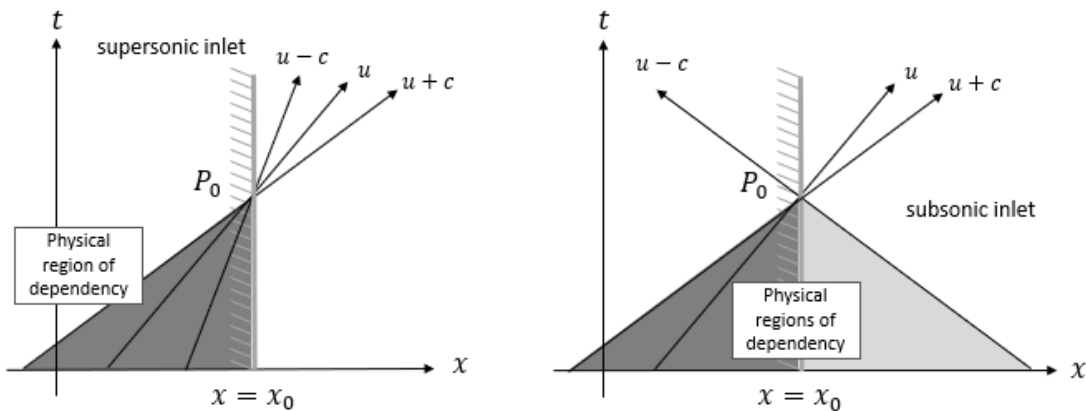


FIGURE 2.1 – Boundary condition for one-dimensional inlet for Euler Equations with the internal (gray) and external (dark gray) physical regions of dependency [1].

Figure 2.1 illustrates the (x, t) plane around an arbitrary inlet point P_0 located at $x = x_0$ for the supersonic and subsonic cases. The former has all waves entering the domain once $u > c$ and consequently $u - c$ is positive. Therefore, the physical region of dependency propagates from the outside of the domain and, thus, all characteristics variables of \mathbf{W} must be given. On the other hand, for the subsonic inlet situation, the wave whose velocity is $u - c$ comes from the inside of the domain and, for this reason, it can not be known beforehand. For the subsonic case, only the characteristics related to u and $u + c$ wave velocities must be imposed at the inlet boundary. The contributions associated with the wave with speed $u - c$ must be extrapolated

from the inside.

For supersonic inlet, the primitive properties associated with the characteristics variables for u , $u - c$, and $u + c$ that are commonly chosen to be imposed are the free-stream pressure and velocity or an analytical solution when applied. Moreover, for the subsonic inlet, the velocity component is extrapolated from the interior domain.

2.4.3 Outlet

At an outlet boundary, analogously to the inlet boundary condition, the information dependency in the (x, t) plane can also be illustrated. For the supersonic outlet, since all the region of dependency is inside of the domain, the properties must be extrapolated from the interior. On the other hand, for the subsonic outlet, commonly the static pressure is imposed due to the $u - c$ wave that is entering the domain and the other properties are extrapolated or calculated from the interior values.

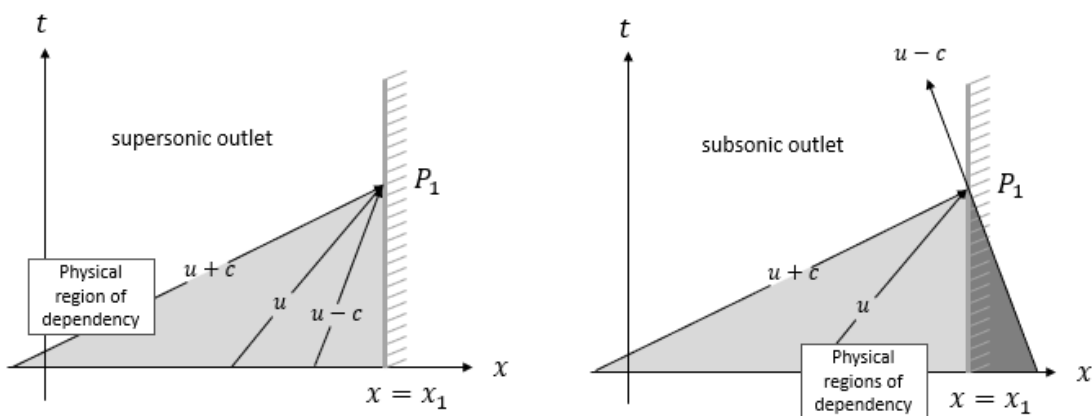


FIGURE 2.2 – Boundary condition for one-dimensional outlet for Euler Equations with the internal (gray) and external (dark gray) physical regions of dependency [1].

2.4.4 Non-Reflective Farfield

By imposing values at the inlet and outlet when solving the Euler Equations, any wave that reaches these boundaries is reflected and stays inside the domain until the numerical dissipation damps its intensity. A simple solution is to expand the external boundary increasing the domain of the simulation so that the path where the wave propagates is sufficiently far that the numerical dissipation can indeed attenuate its magnitude before it arrives at the boundaries. Nonetheless, this methodology increases the computation cost once the simulation domain can become unfeasibly large. Another possible outcome for this problem is to properly impose the characteristics using the Riemann invariants approximating the 1D local solution for the characteristic problem normal to the boundary walls.

2.5 Non-Dimensionalization

The primitive properties of a fluid such as density, pressure and velocity can be represented in several different units and scales. For instance, a density field could range from $10^0 - 10^1 \frac{kg}{m^3}$ while a pressure field from $10^5 - 10^6 \frac{kg}{m.s^2}$, i.e., around 6 orders of magnitude higher than the density. From a numerical perspective, since only a discrete sample of real numbers can be processed in a computer, a wide numerical range of the properties in terms of the order of magnitude can cause high truncation errors and affect the numerical solution. Consequently, the numerical scale which a model is being iterated is relevant to the simulation output and for this purpose a non-dimensionalization procedure of the fluid properties is necessary. The most common approach is to determine beforehand reference values related to the application and

then to rewrite the governing equations with the normalized properties defined as

$$\bar{t} = \frac{tc_{ref}}{L_{ref}} \quad \bar{L} = \frac{L}{L_{ref}} \quad (2.18)$$

$$\bar{\rho} = \frac{\rho}{\rho_{ref}} \quad \bar{\mathbf{U}} = \frac{\mathbf{U}}{c_{ref}} \quad \bar{p} = \frac{p}{\rho_{ref}c_{ref}^2} \quad (2.19)$$

$$\bar{E} = \frac{E}{\rho_{ref}c_{ref}^2} \quad \bar{T} = \frac{T}{T_{ref}c_{ref}^2} \quad (2.20)$$

where _{ref} subscripted properties represent reference values and in several applications they can refer to the free-stream reference values being subscripted by ∞ symbol instead. The speed of sound, c , can be written in terms of the primitives over the assumption of calorically perfect gas using isentropic relations as

$$c = \sqrt{\left(\frac{\partial p}{\partial \rho}\right)_s} = \sqrt{\frac{\gamma p}{\rho}} = \sqrt{\gamma RT} \quad (2.21)$$

3 Numerical Formulation

3.1 Spectral Difference Method

This section is a brief description of the space and time discretization approaches used in the present work. A more elaborated overview can be found in Refs. [13, 14, 15, 16, 17].

In order to represent the continuous domain of a simulation, sub-domains of the space named cells can be defined and related altogether as a contiguous set of cells named as mesh. The procedure to break down the continuous space and determine how the cells are referenced in the mesh is essential for the solver perspective. In fact, it not only determines how the data can be accessed throughout the simulation, but also how accurate a simulation can be and which kind of physical phenomena it will be capable to represent within the discrete approximation of the space.

In general, the finer a mesh is the higher the resolution of the numerical solution, in particular when discontinuities are presented. Nonetheless, finer meshes can drastically increase the computational cost of the simulation and despite the improvements in the physical representation it may be unfeasible for real applications.

3.1.1 Discretization

The space discretization procedure of the governing equations throughout all simulations in this work is made by a high-order Spectral Difference method (SD) [14, 17]. The formulation can properly handle quadrilateral cells given an arbitrary solution accuracy order in an efficient manner by transforming each cell from its physical x, y domain into a particular computational ξ, η domain over the interval $[-1, 1]$ allowing high-order solution interpolation as presented in Refs. [14, 15]. The governing equations in the physical space are then transformed into the computational space and rewritten as

$$\frac{\partial \tilde{Q}}{\partial t} + \frac{\partial \tilde{F}}{\partial \xi} + \frac{\partial \tilde{G}}{\partial \eta} = 0, \quad (3.1)$$

or in its divergence form as

$$\frac{\partial \tilde{Q}}{\partial t} + \nabla_{\xi, \eta} \cdot \tilde{\mathbf{F}} = 0. \quad (3.2)$$

where the conservative variables in the computational space are defined by $\tilde{Q} = |J| Q$, the flux vector $\tilde{\mathbf{F}} = |J| [J]^{-1} \mathbf{F}$, \mathbf{F} is flux vector in the physical space, and J is the Jacobian matrix of the coordinate transformation given by

$$J = \begin{pmatrix} x_\xi & x_\eta \\ y_\xi & y_\eta \end{pmatrix}. \quad (3.3)$$

3.1.2 Space Transformation

The coordinate transformation permits a high-order quadrilateral representation for curved boundaries by considering N equally spaced nodes in the quadrilateral computational space to construct the space transformation Jacobian matrix. The space projection from the physical to the computational space for each quadrilateral can be computed by

$$x(\xi, \eta) = \sum_{m=1}^{(N+1)^2} L_m^{N+1}(\xi) L_m^{N+1}(\eta) x_m \quad (3.4)$$

$$y(\xi, \eta) = \sum_{m=1}^{(N+1)^2} L_m^{N+1}(\xi) L_m^{N+1}(\eta) y_m \quad (3.5)$$

where m goes through all nodes of a N -th order quadrilateral and L^{N+1} is the $(N+1)$ -th order Lagrange polynomial basis, i.e,

$$L_m^{N+1}(\xi) = \prod_{k=1, k \neq m}^{N+1} \frac{(\xi - \xi_k)}{(\xi_m - \xi_k)}. \quad (3.6)$$

3.1.3 Base Polynomials

Furthermore, two sets of intra-cell grid points are allocated, named as solution points (SP) and flux points (FP). The former set storages the nodal values of the conserved variables Q and are located at the Gauss-Legendre quadrature points. The latter storages the nodal values of the flux vectors F and G splitted in two flux point groups located at a combination of the Gauss-Legendre and Gauss-Legendre-Lobatto roots to achieve a stable method according to

Ref. [16, 20]. Figure 3.1 illustrates the cell domain transformation as well as the intra cell grid disposal.

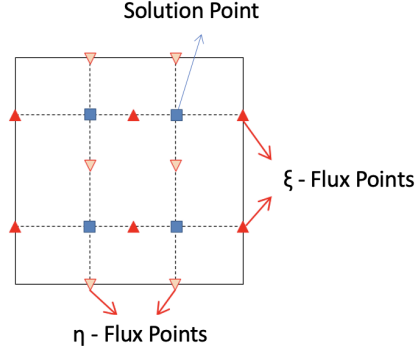


FIGURE 3.1 – Quadrilateral in computational space for 2nd-order Spectral Differences, $p = 1$.

The conserved solution can then be constructed at any target position within the cell computational domain by a nodal interpolation using a Lagrange polynomial basis as

$$\tilde{Q}_i(\xi, \eta) = \sum_{j=1}^{N_p} L_j^p(\xi) L_j^p(\eta) \tilde{Q}_{i,j} . \quad (3.7)$$

where i is the i -th cell index, j the j -th solution point at the i -th cell, N_p the number of basis functions required to construct a p order of the polynomial interpolation, and L^p is the p -th order Lagrange polynomial basis.

3.2 Riemann Solver

The solution vector \mathbf{Q} at the flux points is computed through an interpolation by Eq. 3.7 and since its value is only contiguous within the cell domain, solution discontinuities at the cell interfaces can emerge during the simulation. Hence, the normal flux at the edges flux points is then reconstructed through a Riemann solver, which for all simulations of this work used a Roe

scheme [21]. Since only the normal component can affect the conservation properties through the cells interface, the tangential part of the flux is averaged. The basic formulation for the flux reconstruction can be written as

$$\tilde{F}_n = \frac{1}{2} \{ (\tilde{F}_R + \tilde{F}_L) \cdot \mathbf{n} - |A| (\tilde{Q}_R - \tilde{Q}_L) \}. \quad (3.8)$$

where L and R subscripts represent respectively the left and right cells of an edge and $|A|$ is a representation of the Jacobian matrix of the flux vector which for Roe scheme is assumed to be constant between the two cells at the interface. The Roe matrix $|A_{Roe}|$ is

$$\begin{bmatrix} 0 & n_x & n_y & 0 \\ (\gamma - 1)\tilde{e}_k n_x - \tilde{u}_x \tilde{u}_n & \tilde{u}_n - (\gamma - 2)\tilde{u}_x n_x & \tilde{u}_x n_y - (\gamma - 1)\tilde{u}_y n_x & (\gamma - 1)n_x \\ (\gamma - 1)\tilde{e}_k n_y - \tilde{u}_y \tilde{u}_n & \tilde{u}_y n_x - (\gamma - 1)\tilde{u}_x n_y & \tilde{u}_n - (\gamma - 2)\tilde{u}_y n_y & (\gamma - 1)n_y \\ [(\gamma - 1)\tilde{e}_k - \tilde{h}]\tilde{u}_n & \tilde{h}n_x - (\gamma - 1)\tilde{u}_x \tilde{u}_n & \tilde{h}n_y - (\gamma - 1)\tilde{u}_y \tilde{u}_n & \gamma \tilde{u}_n \end{bmatrix} \quad (3.9)$$

where n_x and n_y are the components of the unit normal vector n . The properties are Roe-averaged values which can be defined through the left L and right R states at the interface as

$$\tilde{\rho} = \sqrt{\rho_L} \sqrt{\rho_R}, \quad (3.10)$$

$$\tilde{u}_x = \frac{u_L \sqrt{\rho_L} + u_R \sqrt{\rho_R}}{\tilde{\rho}}, \quad (3.11)$$

$$\tilde{u}_y = \frac{v_L \sqrt{\rho_L} + v_R \sqrt{\rho_R}}{\tilde{\rho}}, \quad (3.12)$$

$$\tilde{e}_k = \frac{\tilde{u}_x^2 + \tilde{u}_y^2}{2}, \quad (3.13)$$

$$\tilde{u}_n = \tilde{u}_x n_x + \tilde{u}_y n_y, \quad (3.14)$$

$$\tilde{h} = \frac{h_L \sqrt{\rho_L} + h_R \sqrt{\rho_R}}{\tilde{\rho}}, \quad (3.15)$$

The Roe scheme considers the characteristics decomposition, *i.e.*, the decomposition of the Roe matrix into waves and, then, a diagonalization of the matrix is provided such that $|A_{Roe}| = T|\Lambda|T^{-1}$. Equation 3.8 can be rewritten as

$$\tilde{F}_{Roe_n} = \frac{1}{2} \{ (\tilde{F}_R + \tilde{F}_L) \cdot \mathbf{n} - T|\Lambda|T^{-1}(\tilde{Q}_R - \tilde{Q}_L) \}. \quad (3.16)$$

where the matrices T and T^{-1} represent the eigenvectors and Λ , a diagonal matrix with the Roe eigenvalues given by

$$\tilde{\lambda}_1 = \tilde{u}_n, \quad (3.17)$$

$$\tilde{\lambda}_2 = \tilde{u}_n, \quad (3.18)$$

$$\tilde{\lambda}_3 = \tilde{u}_n + \tilde{c}, \quad (3.19)$$

$$\tilde{\lambda}_4 = \tilde{u}_n - \tilde{c}, \quad (3.20)$$

where $\tilde{c} = \sqrt{(\gamma - 1)(\tilde{h} - \tilde{e}_k)}$. From Eq. 3.16, the $\tilde{\lambda}_\ell$ eigenvalues are the wave speeds of the approximate Riemann problem, while the characteristic variables represent the wave amplitudes which can be determined by

$$W = T^{-1}\tilde{Q}. \quad (3.21)$$

therefore, the Roe scheme applied to the second term of Eq. 3.8 becomes

$$T\Lambda(W_R - W_L) = \sum_{k=1}^m \tilde{\alpha}_i |\lambda_i| \tilde{T}^{(k)}. \quad (3.22)$$

where $\tilde{\alpha}_i$ are the wave strength parameters obtained by projecting the jump in the characteristics properties $\Delta W = (W_R - W_L)$ onto the T eigenvector. The projected matrix represented by \tilde{T}

can be defined as

$$\tilde{T} = \begin{bmatrix} 1 & 0 & 1 & 1 \\ \tilde{u}_x & n_y & \tilde{u}_x + \tilde{c}n_x & \tilde{u}_x - \tilde{c}n_x \\ \tilde{u}_y & -n_x & \tilde{u}_y + \tilde{c}n_y & \tilde{u}_y - \tilde{c}n_y \\ \tilde{e}_k & \tilde{u}_x n_y - \tilde{u}_y n_x & \tilde{h} + \tilde{c}\tilde{u}_n & \tilde{h} - \tilde{c}\tilde{u}_n \end{bmatrix} \quad (3.23)$$

In Eq. 3.22, the $\tilde{T}^{(k)}$ represents the k -th column of the projected matrix \tilde{T} defined in Eq. 3.23. Furthermore, the wave strength parameters can be defined as

$$\tilde{\alpha}_1 = \Delta\tilde{\rho} - \frac{\Delta\tilde{p}}{\tilde{c}^2}. \quad (3.24)$$

$$\tilde{\alpha}_2 = \tilde{\rho}\Delta\tilde{u}_t. \quad (3.25)$$

$$\tilde{\alpha}_3 = \frac{\Delta\tilde{p} + \tilde{\rho}\tilde{c}\Delta\tilde{u}_n}{2\tilde{c}^2}. \quad (3.26)$$

$$\tilde{\alpha}_3 = \frac{\Delta\tilde{p} - \tilde{\rho}\tilde{c}\Delta\tilde{u}_n}{2\tilde{c}^2}. \quad (3.27)$$

where the Δ symbol represents a jump condition defined by $\Delta() = ()_R - ()_L$ and $\tilde{u}_t = \tilde{u}_x n_y - \tilde{u}_y n_x$. The Roe scheme provides an exact solution to an approximation of the exact Riemann problem at cell interfaces, that can produce a non-physical expansion wave for stationary expansions and then a well-known phenomenon named Carbuncle can occur. The reason is that the Roe scheme does not introduce artificial dissipation for sonic points. An entropy correction established by Harten in Ref. [22] overcomes this problem by modifying the 3rd and 4th eigenvalues from Eqs. 3.19 and 3.20 by

$$\tilde{\lambda}_\ell = \begin{cases} \tilde{\lambda}_\ell, & \text{if } \tilde{\lambda}_\ell > \delta \\ \frac{\tilde{\lambda}_\ell^2 + \delta^2}{2\delta}, & \text{if } \tilde{\lambda}_\ell \leq \delta \end{cases} \quad (3.28)$$

where δ is a small value which is recommended to be taken as a fraction of the local speed of sound. For the present work, $\delta = \frac{1}{10}$ [23].

Moreover, the flux vectors are computed for each flux point by Eq. 2.10. At the cell interfaces, each flux vector component is reconstructed using the aforementioned approximate Riemann solver in order to obtain a continuous flux between neighboring cells. Then, the reconstructed flux divergence can be interpolated from the set of flux points, similarly to Eq. 3.7, as

$$\nabla \cdot \tilde{\mathbf{F}}_i(\xi, \eta) = \sum_{j=1}^{N_{p+1}} \nabla L(\xi, \eta) \cdot \tilde{\mathbf{F}}_{i,j} . \quad (3.29)$$

where j is the j -th flux point of the i -th cell, $\tilde{\mathbf{F}}$ is the flux vector, and L represents the Lagrange polynomial basis. The superscript N_{p+1} indicates that, for each flux component, the interpolation is one order higher than the solution interpolation described in Eq. 3.7. In this manner, the flux vector divergence provides the same p -th polynomial order representation as the solution vector.

At the end, the solution is computed by the discretized governing equation written as

$$\frac{\partial \tilde{Q}_{i,j}}{\partial t} + \sum_{k=1}^{N_{p+1}} \nabla L(\xi_j, \eta_j) \cdot \tilde{\mathbf{F}}_{i,k} = 0 . \quad (3.30)$$

3.3 Time Integration

The time integration method is an important step to achieve proper results and accuracy when using high-order spatial discretizations. In polynomial-based schemes as the Spectral Difference, the method order increases the number of points in the flux reconstruction procedure and, consequently, increases the size of the spatial matrix operator. In explicit time-marching methods, typically only matrix-vector products are necessary to advance in time. In contrast,

implicit methods are based on solving a system of equations per time step. Although, efficient implicit methods have been proposed in the literature [24] for high-order discretization schemes, they are still more challenging to implement than explicit methods. Thus, for the sake of simplicity, in the present work only an explicit time-marching algorithm is used.

The most common candidate in this scenario is the class of explicit Strongly-Stability Preserving (SSP) Runge-Kutta schemes [25, 26]. Explicit time-marching schemes can be overwhelming due to its limitations of stable time step size and, therefore, making the simulation too long and time consuming. Hence, a 3rd-order SSP Runge-Kutta scheme is chosen to allow a larger time step and a higher accuracy. This time-marching procedure can be given by

$$\tilde{Q}^{(1)} = \tilde{Q}^n + R(\tilde{Q}^n)\Delta t, \quad (3.31)$$

$$\tilde{Q}^{(2)} = \frac{3}{4}\tilde{Q}^n + \frac{1}{4}[\tilde{Q}^{(1)} + R(\tilde{Q}^{(1)})\Delta t], \quad (3.32)$$

$$\tilde{Q}^{(3)} = \frac{1}{3}\tilde{Q}^n + \frac{2}{3}[\tilde{Q}^{(2)} + R(\tilde{Q}^{(2)})\Delta t]. \quad (3.33)$$

where the \tilde{Q} is the solution vector of the conservative variables over the set of solution points in the computational space. The $R(\tilde{Q})$ is the residue of the spatial discretization as a function of the solution vector \tilde{Q} . The Δt is the time step which can be defined as

$$\Delta t = CFL \frac{\Delta x}{|U_\infty + c_\infty|(2p + 1)}. \quad (3.34)$$

where the CFL is the Courant-Friedrichs-Lowy condition, Δx is a reference value for the cell size, $U_\infty + c_\infty$ is the reference value for the highest speed in the simulation domain as a function of the free stream velocity U_∞ and free stream speed of sound c_∞ , and p the order of

the polynomial interpolation.

3.4 Evaluation Metrics

3.4.1 Residue

For steady flows, the time integration of the numerical solution is expected to converge to some nearly-zero rate of change in time, i.e., the numerical order of accuracy is represented by the residue vector magnitude R which is bounded to the solver resolution or even the machine error. In general, the residue is presented and compared by its L2-norm order as a function of time or number of iterations. The log10 of the L2-norm order is given by

$$\log_{10}(|R|_2) = \log_{10} \left(\sqrt{\frac{1}{N} \sum_{i=1}^N R_i^2} \right), \quad (3.35)$$

where N is the number of cells and the R_i is the i -th cell residue calculated as the average residue of its solution points.

3.4.2 Isentropic Flows

From the second law of thermodynamics, entropy variations are presented in two different scenarios when discontinuities are presented in the domain such as shock wave and in flows where vorticity exists. Thus, the entropy is a common candidate to measure the behavior of the aforementioned phenomena and even as an error indicator for isentropic flows.

The entropy, using the isentropic relations, can be given by

$$S = \frac{p}{\rho^\gamma}. \quad (3.36)$$

where p is the fluid pressure, ρ the density, and γ is the fluid isentropic coefficient.

3.4.3 Analytical Solution Error

In the presence of an analytical solution, a suitable and desirable evaluation metric is by comparing it with the numerical solution. Several approaches can be provided, however, throughout the present work a L2-norm is chosen. The analytical solution error can, then, be determined by

$$\text{Error} = \sqrt{\frac{1}{N} \sum_{i=1}^N (sol_i - sol_{analytical_i})^2}. \quad (3.37)$$

where N is the number of cells, sol_i and $sol_{analytical_i}$ are, respectively, the i-th cell numerical and analytical solution calculated as the average value of its solution points.

4 Conservative High-Order Interpolation

In this chapter details are provided about the methodology used in the present work to implement an overset grid solver. As a high-level overview, the consideration of overset grids here is based on two main steps: a geometric search and a data communication step. The former generates a tree-based data structure for the mesh nodes which is used to classify the cells around the overset region establishing a receptor-donor relationship. The latter details a conservative high-order approach for the data interpolation and a methodology to impose the interpolated solution throughout the numerical solution.

4.1 Overset Grids

Generally the most common setup for an overset grid system in Computational Fluid Dynamics applications involves a distinct set of meshes: a background and a near-body mesh [9]. The near-body mesh has a solid body inside and is embedded into a typically much larger mesh, the background mesh. Due to the difference in the physical scale, this configuration eventually provides a considerable processing cost reduction during the simulation in particular for moving boundary applications, since only the near-body mesh has to be re-meshed when the body moves or is deformed as discussed in Refs. [27, 28, 29]. In order to solve the time advancement

of the numerical solution, data must be shared within the outer boundary of the near-body mesh and the overset region inside the background mesh so that it preserves the conservative properties of the fluid. Figure 4.1 illustrates the mesh setup where the near-body mesh is in orange while the background one is illustrated in black.

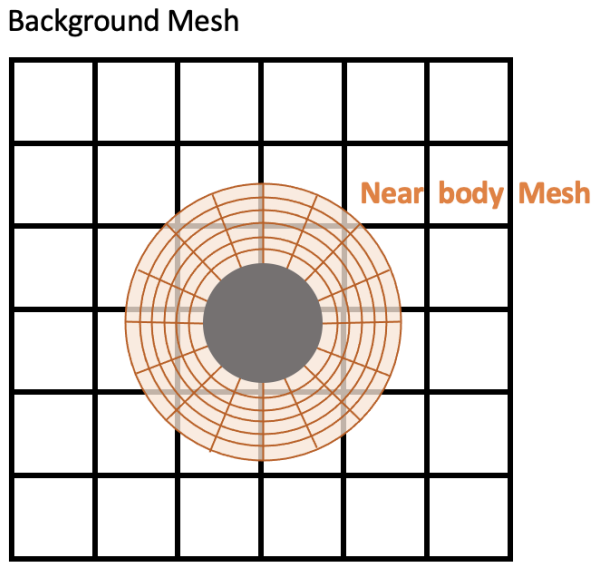


FIGURE 4.1 – Overset meshes setup: background mesh in black and near-body mesh in orange.

4.2 Overset Assembly

4.2.1 Geometric Search

The definition of a receptor-donor relationship is necessary to communicate data from cells in the background mesh to nodes over the external boundary in the near-body mesh. Additionally, some cells in the background mesh may be completely overlapped by the near-body mesh domain and, thus, a procedure to remove these cells from the solver iterations should be performed. This procedure is commonly referred as the hole-cutting process [29, 27].

In order to simplify both applications, two types of cells are defined: fringe cells and hole cells. Fringe cells will receive, communicate and process data during the solver iterations, while hole cells are skipped with no equation being solved. Hole cells are background cells which are fully emerged at the overset region between the meshes. Thus, the hole cell area solution is only calculated at the near-body mesh cells that overlap it.

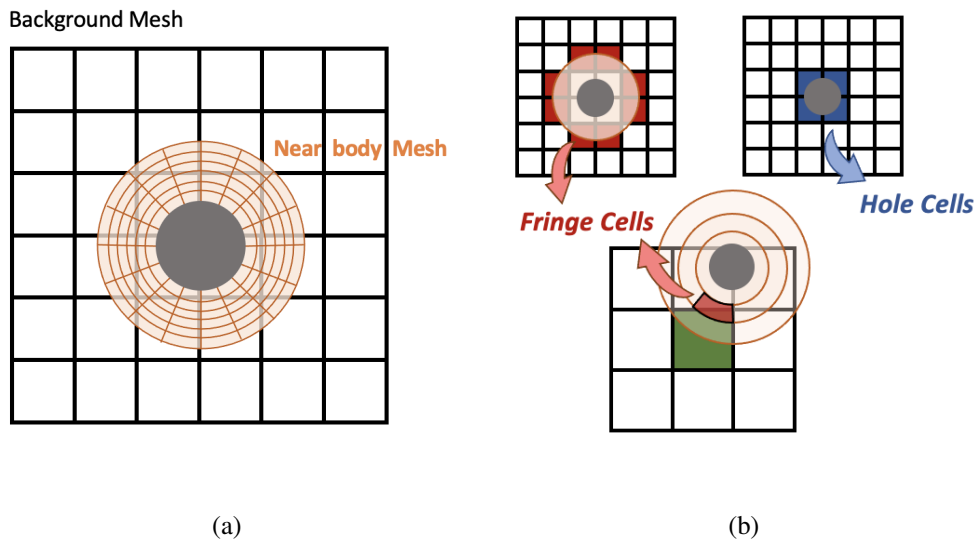


FIGURE 4.2 – Overset grid setup and cell type definitions for a illustrative cylinder example.

Figure 4.2 illustrates the setup of background and near-body meshes and the location of some fringe and hole cells. Figure 4.2(a) shows the overset meshes setup with the near-body mesh in orange and the background mesh in black. Figure 4.2(b) illustrates the definition of the cell types where the fringes (in red) are used to interpolate solution while holes (in blue) bypass the solver. The green cell is the same fringe cell in red as before, but changed to emphasize near-body fringes. Note that no hole cells are defined for the near-body mesh which means that the solution is calculated for all of its cells at each time step. However, the fringe cells can exist in both meshes and used as donor or receptor for the data communication.

The geometric search problem applied to the context of overset grids aims to define an

efficient manner of finding which cell in the donor mesh embeds a specific coordinate in the receiver mesh. In the present work, the kD-tree algorithm described in Ref. [30] is used for this purpose requiring a tree data structure for the node vectors in both meshes. This tree representation is well suited for the application due to its logarithmic time complexity, which essentially yields a splitting of the domain by half in each search step, according to Ref. [31].

Figure 4.3 illustrates the tree structure in the fluid domain where the dots represent the cell vertices, the blue lines are the x-axis splits of domain, and the orange lines are the y-axis splits of domain. The kD-tree algorithm is built upon all cell vertices and the Fig. 4.3 is only illustrating some vertices for the sake of simplicity. For each split, the median value of one axis is selected so that the nodes in tree structure split the domain in half at each tree depth.

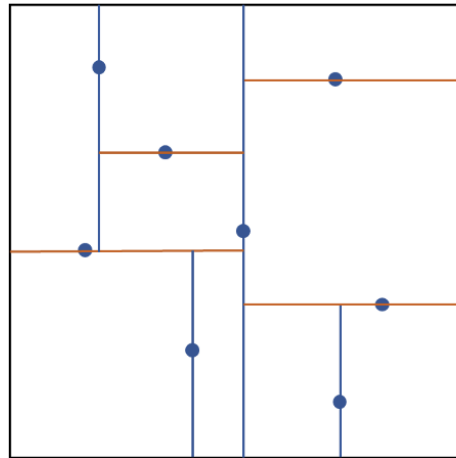


FIGURE 4.3 – kD-tree geometrical view for a given set of points.

The kD-tree structure is build for both the background and near-body nodes and a look-up method of finding the nearest node to a given coordinate is implemented over the tree data structure. The look-up in the kD-tree is done recursively and can be described, for 2-D, in the steps:

- A target coordinate is given.
- Select a dimension sequentially in alternate cycles between x and y . The nodes of the kD-tree are chosen as the approximate median value of the k th-coordinate of the given domain following this alternate dimension cycles. Therefore, at each kD-tree searching step approximately half of the nodes are eliminated from candidate.
- Initially, select the root node as candidate for the nearest node of the testing mesh to the target node.
- Calculate the distance between the candidate and the target and store it as the current radius that limits the area where the nearest node can be, as shown in Fig. 4.4.
- Compare the selected axis value of the target with the candidate node and check whether the candidate coordinate satisfy the conditions:

$$\text{target}_{k\text{-axis}} \leq \text{candidate}_{k\text{-axis}} \text{ OR } (\text{target}_{k\text{-axis}} - \text{radius}) < \text{candidate}_{k\text{-axis}}$$

$$\text{target}_{k\text{-axis}} > \text{candidate}_{k\text{-axis}} \text{ OR } (\text{target}_{k\text{-axis}} + \text{radius}) > \text{candidate}_{k\text{-axis}}$$

- If the first condition is satisfied, repeat the search process with the candidate's right child as the new candidate.
- If the second condition is satisfied, repeat the search process with the candidate's left child as the new candidate.
- Compare the minimum distances from both outputs from the left and right sides and finally determine the nearest node to the target.

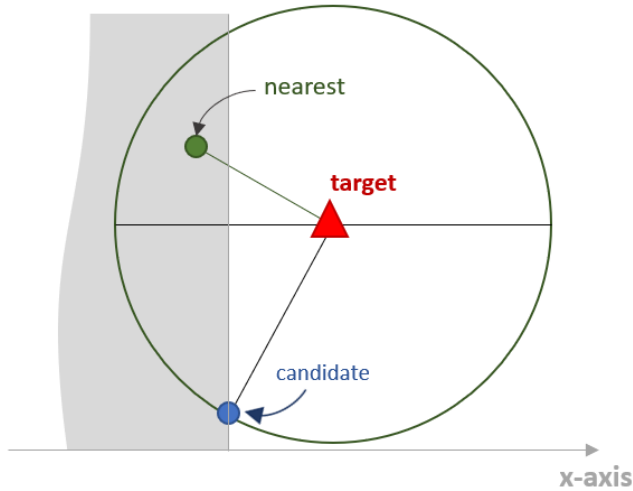


FIGURE 4.4 – kD-tree radius test.

4.2.2 Receptor-Donor Connectivity

The Spectral Difference method, selected in the present work as the spatial discretization method for the governing equations, defines a specific set of points to interpolate the flux vector within the cell domain. Some of these flux-points are located at the cell interfaces and are used to correct the flux discontinuities between neighboring cells. In particular, at the outer and inner boundary interfaces, since the cells at these locations have no neighbor cells, ghost cells are generated containing a mirror of the interface flux-points of the boundary cells. The flux points of the ghost cells are the target coordinates used in the geometric search to map the fringe and initial hole cells.

At the end of the geometric search process of the boundary flux-points, the nearest node from the donor mesh is found and an additional step is necessary to determine whether the cell, that owns the nearest node, in fact embeds the flux-point. For each cell candidate, a loop throughout its edges is done checking whether the receiver node is inside the candidate cell by

validating the sign of the cross product between the edge and the target node, as illustrated in Fig. 4.5(b). The donor-receiver neighborhood in the physical space is shown in Fig. 4.5(a).

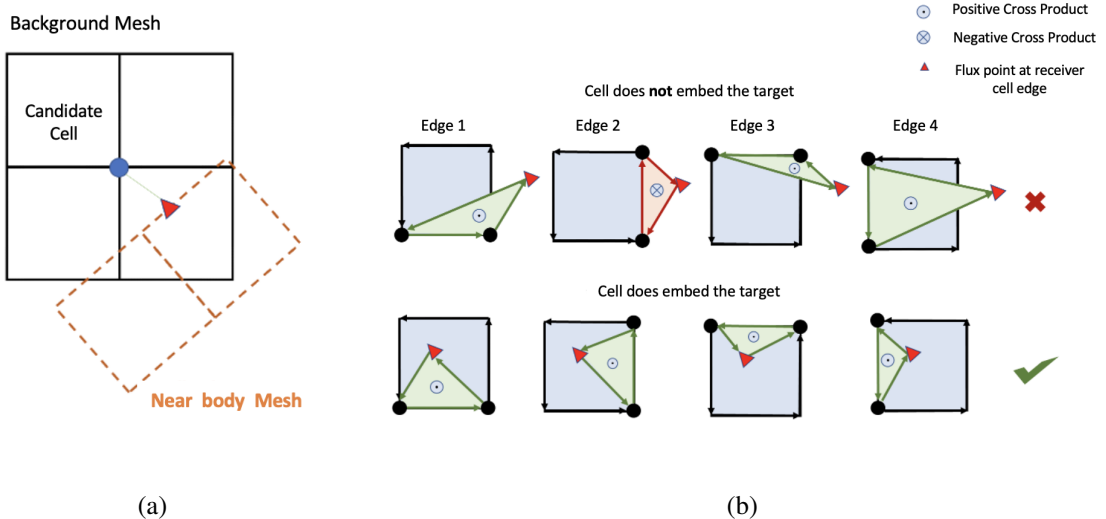


FIGURE 4.5 – Donor cell searching procedure given the target node (red triangle) and the nearest donor node (blue circle). The failed test is done over the left bottom cell and the successful test over the right bottom cell.

If all the cross product signs are positive over the counter-clockwise direction, the cell candidate is embedding the flux-point and a fringe flag is attributed to this cell. The fringe cells are determined for the background mesh by applying this search process for each flux point in the ghost cells at the external boundary of the near-body mesh. Moreover, for the near-body mesh, the fringes are determined from the flux points at the inward facing edges of the background mesh fringes as illustrated in Fig. 4.6.

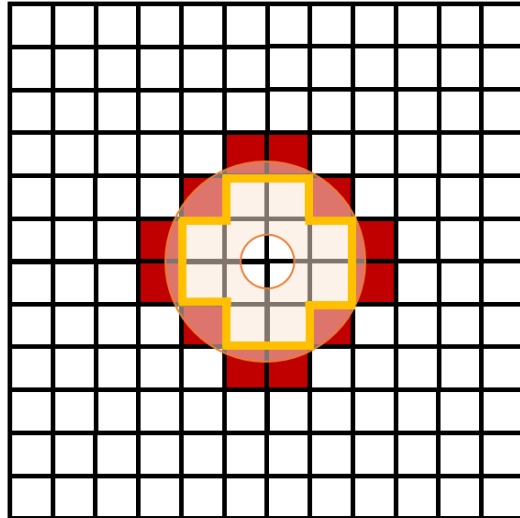


FIGURE 4.6 – Inward facing edges (in yellow) of the fringe cell circuit in the background mesh.

4.2.3 Extension to Curved Meshes

The presented donor cell searching procedure uses the vertex nodes of an edge altogether with the target node to determine whether the target node is inside of a candidate cell through its cross product sign. Although it is well-suited for an arbitrary polygon, i.e., it is not restricted to quadrilateral cells, the methodology can result in false positive donor flag classification around curved cells. Figure 4.7 shows a quadrilateral cell with low-order (orange dots) and high-order nodes (blue squares), respectively at Fig. 4.7(a) and 4.7(b). The dotted curved lines in Fig. 4.7 illustrates the curvature of the geometry of the cell boundary that is interpolated throughout the high-order nodes. Figure 4.7(c) shows the limitation of cell searching procedure when applied only to the vertex nodes and ignoring the edge curvature which can result in a negative cross product over the low-order edge, even though the target node is indeed inside the cell.

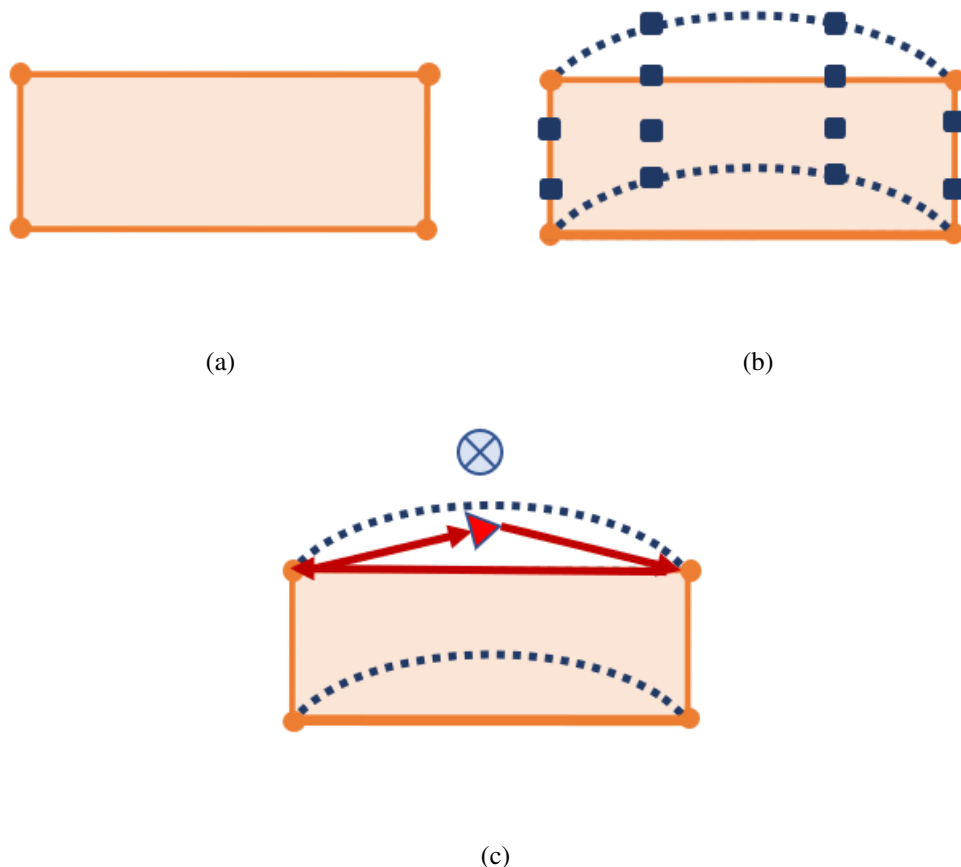


FIGURE 4.7 – Cell searching procedure issue for curved cells.

The extension approach includes the high-order nodes over the edges as if the quadrilateral were an arbitrary polygon so that the information of curvature can be considered leveraging the same cell searching procedure as explained in the receptor-donor relationship section. Figure 4.8 exemplifies the sequence of cell searching procedure using the high-order interface nodes (blue squares) and vertices (orange dots). Commonly the enumeration of high-order nodes in the vector of nodes is posterior to the vertices, i.e., the low-order nodes are counted first. This is relevant for this procedure since it considers the counter-clockwise direction as reference for the sign comparison which, then, requires a simple re-enumeration step for the vector of nodes in each edge.

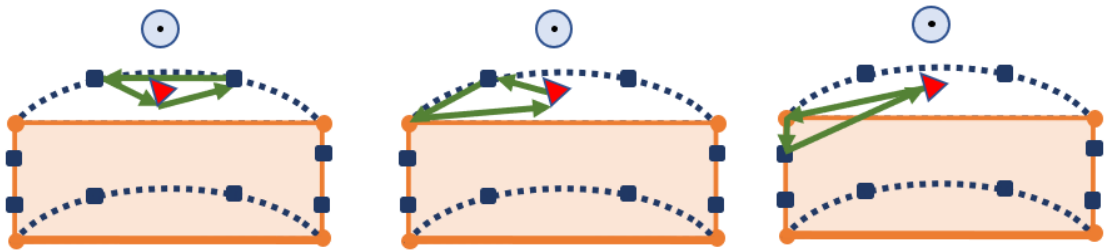


FIGURE 4.8 – High-order edges nodes inclusion in the cell searching procedure.

4.2.4 Hole-Cutting

For the hole cells, a random node in the near-body grid is then selected until its donor cell output in the background satisfy the conditions of not being a fringe and being completely overlapped by the near-body mesh. This cell is flagged as a hole cell and it is used as input for a Breadth-First Search (BFS) algorithm which propagates the hole flag for the unmarked cells until all interior cells within the fringe closed circuit are visited [32]. Figure 4.9 shows a sketch of this procedure where the first hole cells are flagged through an inner boundary or random internal node from the near-body mesh. Then, the child of a hole cell is only stacked to be visited in the next iteration if it is not a fringe cell. At last, new ghost cells are created at the fringe-hole interfaces in order to correct the flux normal to its edges by communicating data from the near-body mesh. The same donor-receiver relationship procedure is done to determine which cells at the near-body mesh embeds all flux points in these ghosts as well.

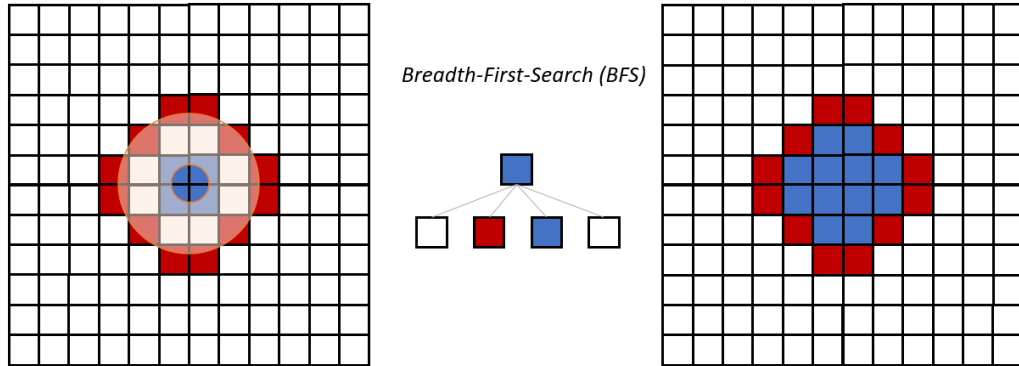


FIGURE 4.9 – Hole-cutting flag (blue) propagation using a Breadth-First Search (BFS) algorithm conditioned by the fringe cell circuit (red).

4.3 Data Communication

4.3.1 Data Interpolation

The first methods to consider overset grids were based on low-order solvers restricted to structured meshes as in the NASA's PEGASUS software [11]. Moreover, the approach for data communication during these first implementations was developed mostly using a bilinear interpolation which can limit the accuracy order of the interpolated solution. Recently, new data communication methodologies have been developed extending some high-order methods in the FR/CPR framework to overcome the limitations of the bilinear interpolation and additionally to consider unstructured overset grids. In order to provide a conservative high-order data communication, two different approaches were developed firstly for Discontinuous Galerkin type methods: the face-based [7] and the element-based approaches [33, 34].

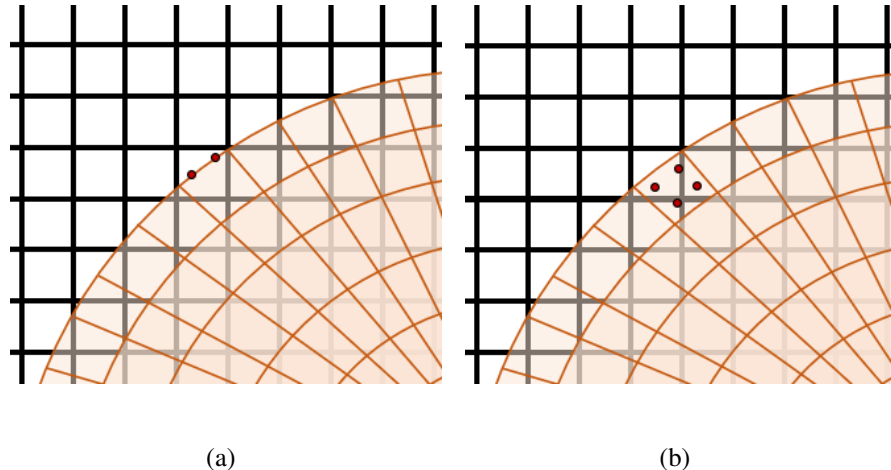


FIGURE 4.10 – Data communication nodes setup at the overset region for face-based and element-based approaches.

In the face-based approach illustrated in Fig. 4.10(a), the solution data is interpolated from the donor cells that embed nodes located at the outer boundary faces around the overset region. The interpolated solution is used to calculate the flux at the interface and is applied as a weak boundary condition in the outer boundary. The Riemann solver can, then, be applied to correct the flux in the overset interfaces [7].

In the element-based approach in Fig. 4.10(b), the solution data is interpolated to internal points of the cells located at the outer boundary. Differently to the face-based approach, the interpolated solution here is used to interpolate the solution within the cell domain and is imposed as the solution in the current iteration step [28].

For the present work, the face-based approach is used due to its simpler implementation and greater robustness in comparison with the element-based, according to Refs. [7, 9].

4.3.2 Standard Space Projection

The cells in the Spectral Difference method are projected to a standard space where the solution can be represented through a nodal interpolation using specific polynomial basis functions. This standard space transformation is unique for each cell and is defined by the cell Jacobian matrix J which is a function of the computational space coordinates ξ, η for curved cells. In the context of data communication, the solution is interpolated from the set of solution points of the donor cell to a target node at the receptor standard space. The target node in the face-based approach is a flux-point whose space coordinates are commonly stored in the computational space of the receptor cell. In order to assemble the data communication, the target coordinates need to be projected from the receptor standard space into the donor standard space so that the solution can be interpolated as illustrated in Fig. 4.11.

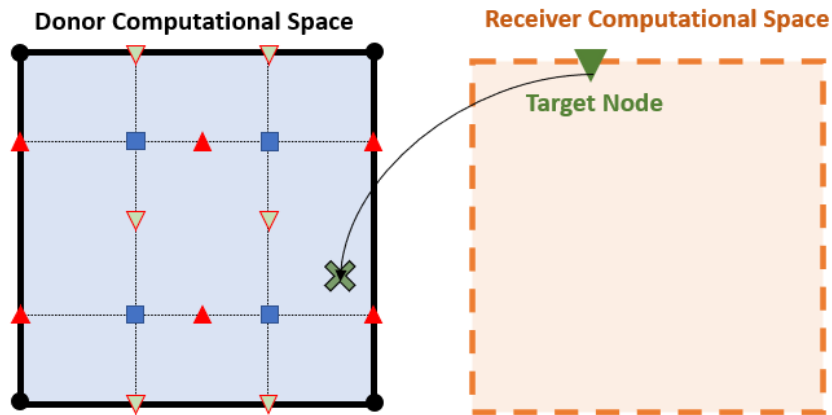


FIGURE 4.11 – The target node is projected from the receiver to the donor computational space.

This coordinate transformation can be done in two steps. First the target coordinate is projected from the receiver computational space to the physical space using Eq. 4.1. Then, this

physical space coordinate is used in Eq. 4.2 to determine the ξ, η coordinates in the donor computational space allowing the interpolation of the solution through Eq. 3.7 as illustrated in Fig. 4.12. Note that a non-linear system of equation has to be solved to find the target ξ, η coordinates in Eq. 4.2. In the present work, a Newton-Raphson solver is used where the function is defined by Eq. 4.2 and its derivative through the Jacobian matrix.

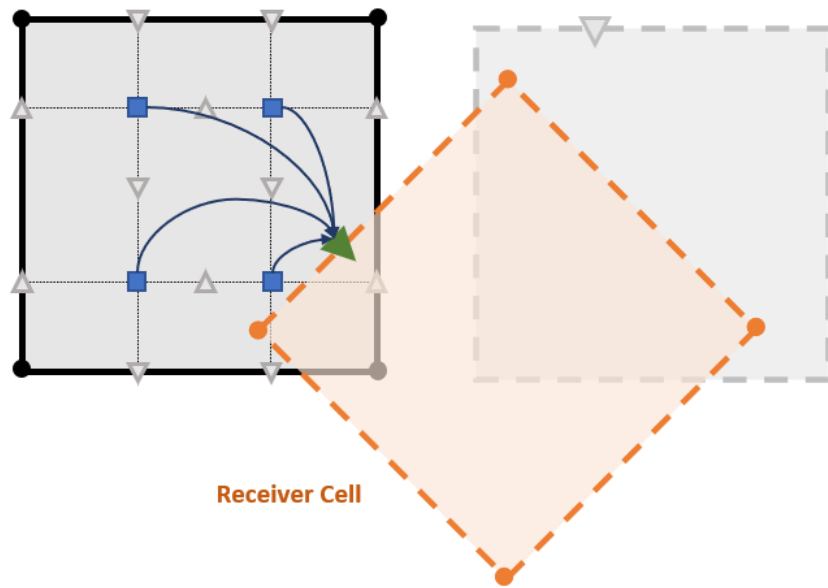


FIGURE 4.12 – The solution is interpolated to the target coordinate inside the donor computational space.

For high-order meshes, the Jacobian matrix of the transformation from the physical to the computational space is not constant within the cell domain, but a function of the target ξ, η coordinates. Therefore, for each Newton-Raphson iteration, the Jacobian matrix has to be computed with the updated guess of the projected target coordinates. The subscript R stands for receiver and D for donor.

$$x_{FP_t} = \sum_{m=1}^{(N+1)^2} L_{Rm}^{N+1}(\xi_{R_{target}}) L_{Rm}^{N+1}(\eta_{R_{target}}) x_{Rm} \quad (4.1)$$

$$\sum_{m=1}^{(N+1)^2} L_D^{N+1}(\xi_{D_{\text{target}}}) L_D^{N+1}(\eta_{D_{\text{target}}}) x_{D_m} = x_{FP_t} \quad (4.2)$$

After the target coordinate is projected to the donor computational space $\xi_{D_{\text{target}}}, \eta_{D_{\text{target}}}$, the solution can be interpolated through Eq. 3.7 preserving the same high-order polynomial representation of the solution used by the Spectral Difference method.

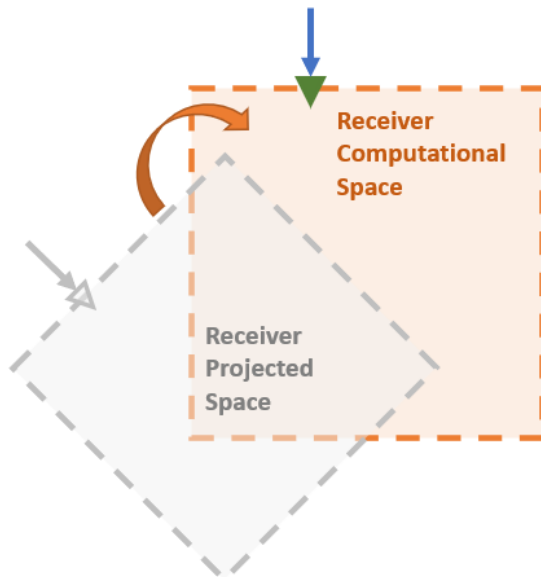


FIGURE 4.13 – The interpolated solution (arrow) is then projected back to the receiver computational space.

The interpolated solution still lies in the donor computational domain and, therefore, needs to be projected back to the receiver computational domain. Figure 4.13 illustrates the space projection step from the donor computational space into the receiver computational space.

First the interpolated solution is projected from the donor computational space to the physical space using the donor Jacobian matrix calculated at the target node. Then, the solution at the physical space is transformed to the receiver computational space through the receiver Jacobian matrix as described in Alg. 1. The interpolated solution in the receiver computational space is imposed as a weak boundary condition for the Riemann solver, i.e., the solution is not imposed

to assume the interpolated value, but instead it is used through a Riemann solver in order to reconstruct a continuous flux at the interfaces by the use of Eq. 3.8. The boundary condition is illustrated in Fig. 4.14.

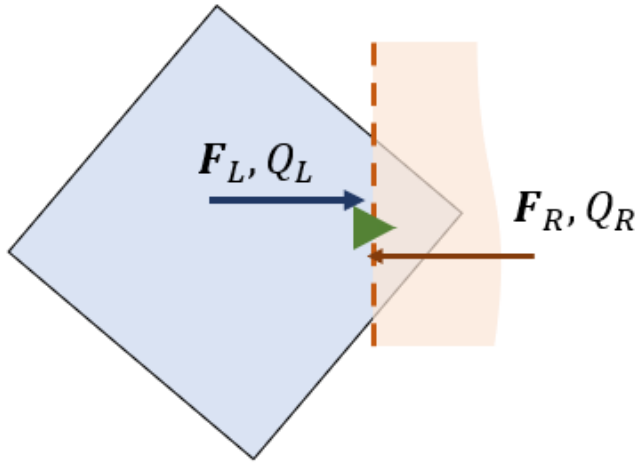


FIGURE 4.14 – Imposition of the interpolated solution as a weak boundary condition using flux reconstruction.

Algorithm 1 Pseudo-code for the interpolated solution projection from the donor to the receiver.

```

1: // Calculate the Donor Jacobian matrix at the target node
2:  $J_{Donor} \leftarrow \text{Donor.CalculateJacobianAtNode}(\xi_{D_{target}}, \eta_{D_{target}})$ 
3:
4: // Transform the solution from computational donor space to the physical space
5:  $Q_{Physical} \leftarrow (\frac{1.0}{J_{Donor}})Q_{Interpolated}$ 
6:
7: // Get the receiver Jacobian matrix at the target flux-point
8:  $J_{Receiver} \leftarrow \text{Receiver.Jacobian}(\xi_{D_{target}}, \eta_{D_{target}})$ 
9:
10: // Transform the solution from the physical space to the computational receiver space
11:  $Q_{Receiver} \leftarrow J_{Receiver}Q_{Physical}$ 

```

5 Results

The results section is divided in three test cases: the Ringleb flow, the inviscid cylinder and the isentropic inviscid vortex. The former is intended to validate the high-order solver capabilities implemented in the present work and the others are used as comparative test cases between the single and overset mesh results. An important notation is used throughout the results section to notify the solver accuracy and mesh orders. For instance, a P2Q2 test considers a 2nd-order reconstruction of cell properties - a parabola, thus the P2 - which yields a 3rd-order accurate Spectral Difference method, with a 2nd-order construction of the quadrilateral mesh, which means that cell edges are parabolas, and thus the denomination Q2.

5.1 Ringleb Flow

The Ringleb flow is a common candidate to state the level of accuracy in high-order solvers due to its analytical solution for the Euler Equations derived from a hodograph transformation [35]. Another interesting property of the Ringleb flow is that the transition from supersonic to subsonic region does not generate a shock, then no limiter is needed. The analytical solution is used as initial condition and only depends on three parameters: the velocity magnitude q and the stream function interval given by $[k_{min}, k_{max}]$. The stream function interval defines the stream

lines for the inner wall, k_{max} , and outer wall, k_{min} . The mesh for the Ringleb flow is defined through the hodograph transformation of the Euler Equations and therefore a relation from the fluid properties to the x, y coordinates is established. The velocity magnitude q varies between q_0 and k , for each k in the interval $k_{min} \leq k \leq k_{max}$. For each velocity magnitude q , the speed of sound a , density ρ , pressure p and quantity M can be defined by

$$a = \sqrt{1 - \frac{\gamma - 1}{2} q^2}; \rho = a^{\frac{2}{\gamma-1}}; p = \frac{1}{\gamma} a^{\left(\frac{2\gamma}{\gamma-1}\right)} \quad (5.1)$$

$$M = \frac{1}{a} + \frac{1}{3a^3} + \frac{1}{5a^5} - \frac{1}{2} \log \frac{1+a}{1-a}. \quad (5.2)$$

where γ is 1.4 for the air. For each pair (q, k) , the mesh coordinate x, y can be determined by

$$x(q, k) = \frac{1}{2p} \left(\frac{2}{k^2} - \frac{1}{q^2} \right) - \frac{M}{2} \quad (5.3)$$

$$y(q, k) = \pm \frac{1}{k\rho q} \sqrt{1 - \left(\frac{q}{k}\right)^2} \quad (5.4)$$

The results obtained in this test case considered $q_0 = 0.5$, $k_{min} = 0.7$ and $k_{max} = 1.5$. The boundary conditions are imposed with a subsonic inlet at the top, a subsonic outlet at the bottom and the exact analytical solution at the inner (left) and outer (right) walls as illustrated in Fig. 5.1(a).

The mesh is gathered from the 4th High-Order CFD Workshop [36] containing 12 fourth-order cells (Q4). As it can be seen in the Ringleb flow boundary conditions illustrated in Fig. 5.1(a), the inflow and outflow area are also curved and, therefore, the Q4 high-order mesh

is chosen to represent it. The initial input mesh for this test case is illustrated in Fig. 5.1(b) representing a Ringleb mesh with $q_0 = 0.5$, $k_{min} = 0.7$ and $k_{max} = 1.5$.

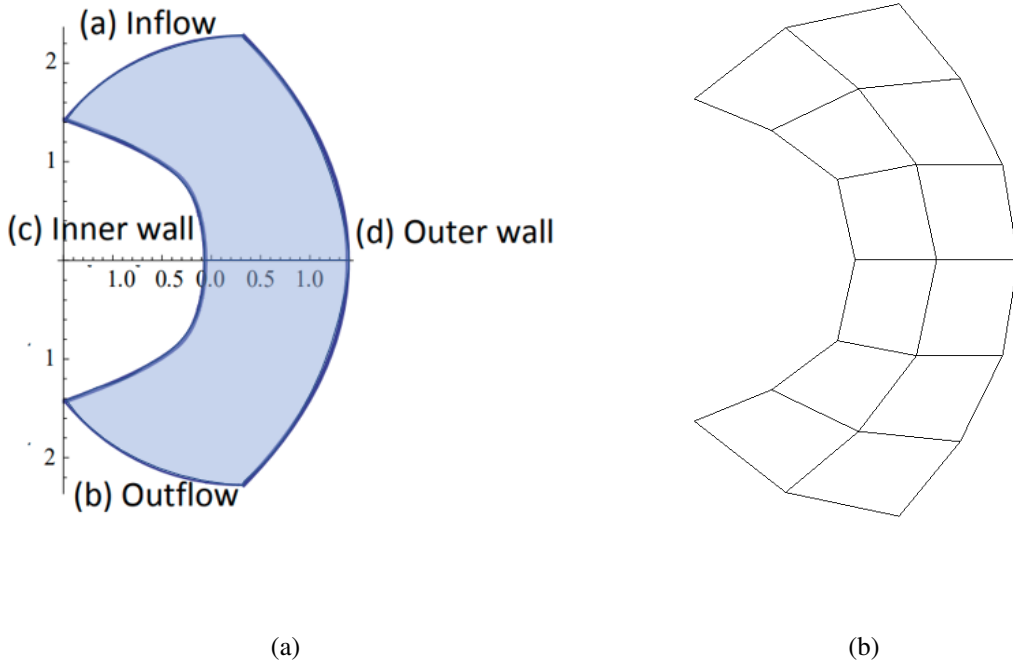


FIGURE 5.1 – Ringleb flow boundary conditions (left) and initial mesh (right).

The Spectral Difference method is used with several polynomial orders ranging from $P = 2$ up to $P = 5$ and Fig. 5.2 shows the correspondent pos-processing mesh and close-up views. The pos-processing mesh is generated through all the cells vertices, solution and flux points with no information lost. Additionally, since only the solution points own the final converged solution, in the pos-processing procedure, the solution is interpolated from the solution points to the flux-points and vertices where an average is applied to smooth the solution. In the close-up images from Fig. 5.2, one may compare the different degrees of freedom between the selected P for the same 12 cell mesh used in the entire test.

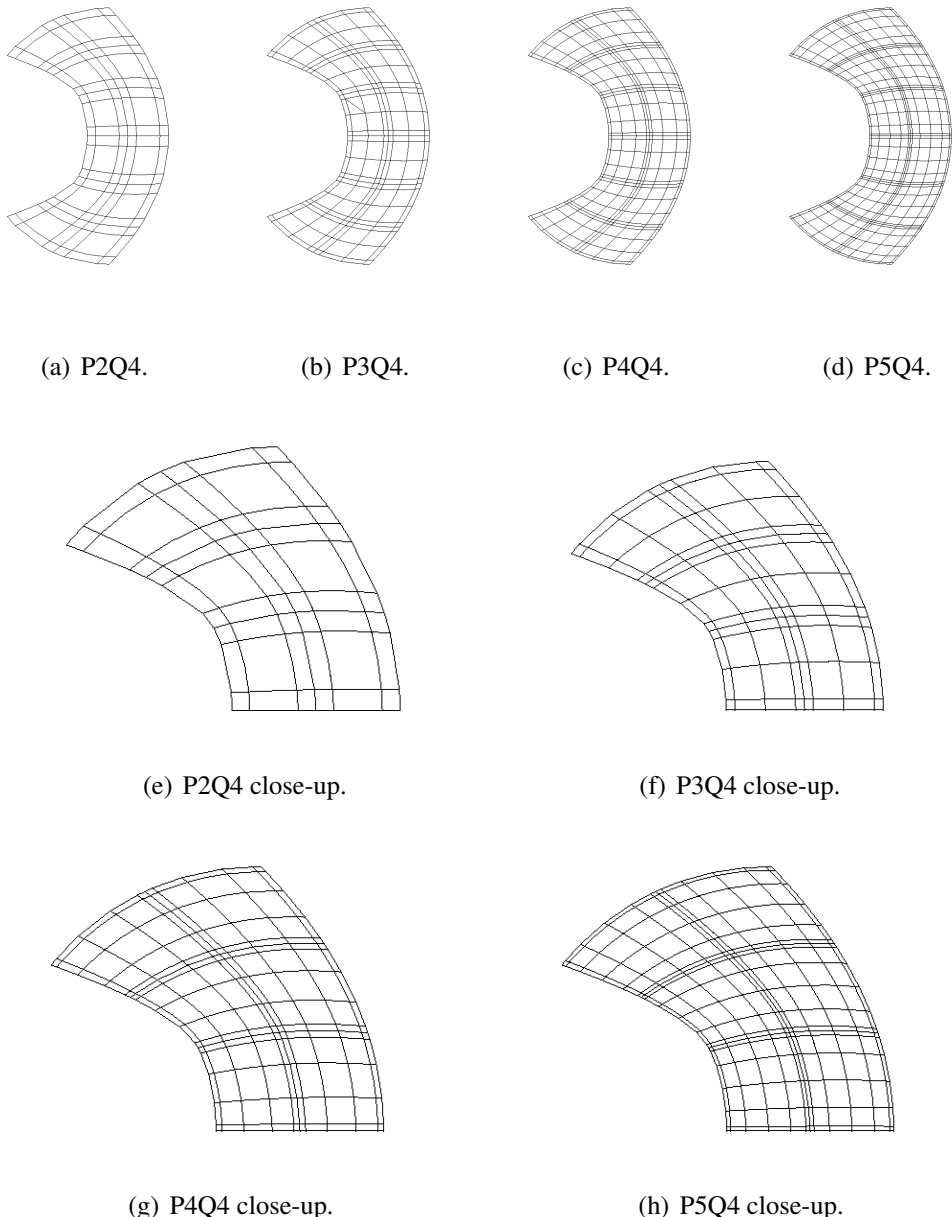


FIGURE 5.2 – Meshes for the Ringleb flow test case for different P values.

The analytical solution is determined by solving Eqs. 5.3 and 5.4 numerically over q with a Newton Raphson algorithm. The analytical values for the velocity components, u and v , are defined by $u = \pm q\cos(\theta)$ and $v = -q\sin(\theta)$, where $\theta = \arcsin\left(\frac{q}{k}\right)$. Additionally, the u velocity component direction changes depending on the y coordinate sign. Figure 5.3 presents the analytical Mach number solution considering $q_0 = 0.5$, $k_{min} = 0.7$ and $k_{max} = 1.5$ with a colormap ranging from 0.5 to 2.0. The analytical Mach number solution shows a symmetrical

solution over the x axis with the presence of supersonic regions, despite no shock is formed and then a smooth solution is expected.

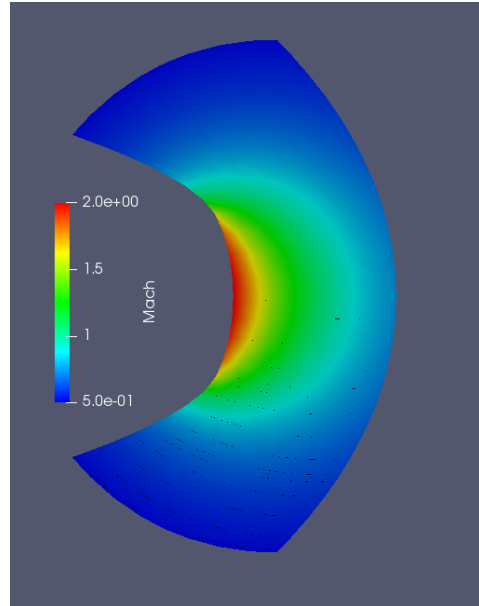


FIGURE 5.3 – Analytical Ringleb flow solution: Mach number contours.

The simulation results for the L2-norm of the density residue are shown in Fig. 5.4 for different orders of the Spectral Difference method. The L2-norm is calculated over all solution points considering the entire residue vector norm, *i.e.*, the residue of all conservative properties. The time integration method is a SSP Runge-Kutta scheme of 3rd order and 3 stages. The time step is fixed for each simulation and it is given by Eq. 3.34. Consequently, for higher values of P , the time step decreases. As it can be seen in Fig. 5.4, the slope of the lines representing the residue order of magnitude rate of change is almost constant for each P value. Additionally, for all test cases, *i.e.*, for all P values, the solution has converged to machine zero error.

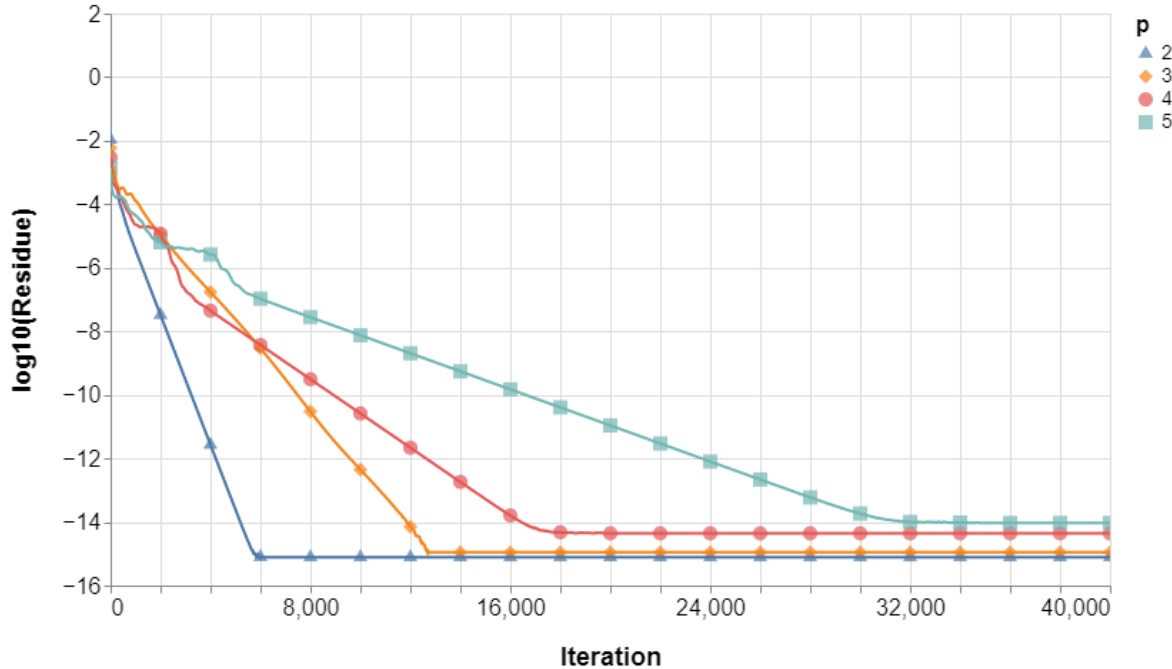


FIGURE 5.4 – L2-norm of the density residue for the Ringleb flow for different values of P for the same mesh (Q4).

The converged Mach number solutions for different P values are presented in Fig. 5.5 containing the field colormap ranging from 0.5 to 2.0 and contours with 0.1 step value. For 2nd and 3rd-order of solution polynomial reconstruction, *i.e.*, $P = 2$ and $P = 3$, despite the fact that convergence to the machine error level has been reached, the Mach number contours in Figs. 5.5(a) and 5.5(b) presented asymmetries with regard to the x-axis and spikes in the colormap close to the outlet, where the velocity magnitude showed higher values than expected according to the provided analytical solution in Fig. 5.3. On the other hand, when the spatial discretization method order is greater or equal to the presented mesh order, the asymmetries are eliminated. As it can be seen in Figs. 5.5(c) and 5.5(d), respectively, for $P = 4$ and $P = 5$ with the 4th order mesh, the numerical Mach number solution captures the shockless supersonic region which can be compared to the analytical solution.

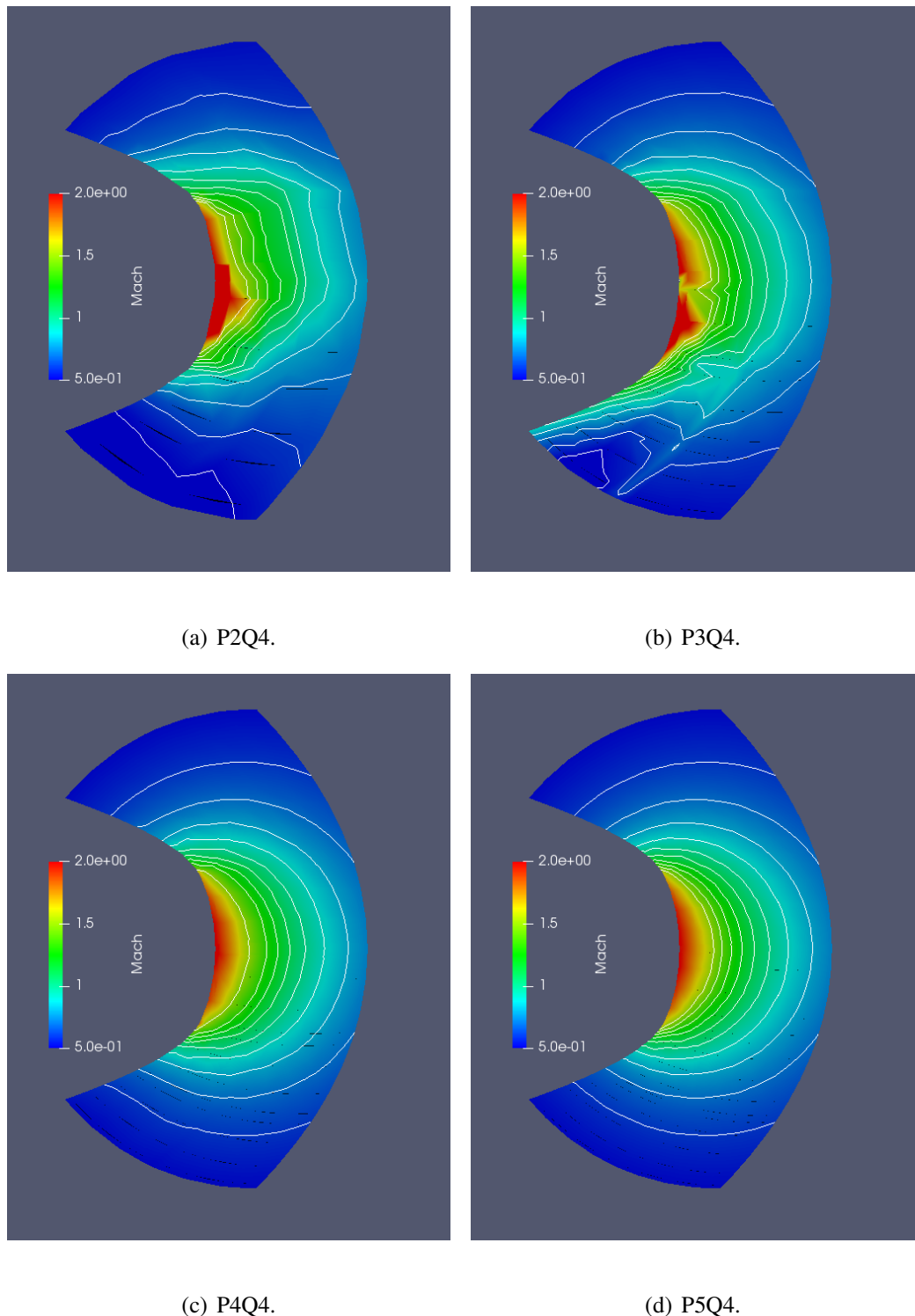


FIGURE 5.5 – Converged numerical Mach number contour solution for the Ringleb flow test case for different P values.

5.2 Inviscid Cylinder

A subsonic inviscid flow over a cylinder is considered to compare the single and overset mesh results. The simulation is setup with a free-stream Mach number of 0.2 in order to observe a double symmetry at the horizontal and vertical axis for the Mach number field solution when solving the Euler equations. The mesh domain is defined with a 100-cylinder radius with the overall initial condition of $Mach = 0.2$, $\rho = 1$ and $p = \frac{1}{\gamma}$ assuming $\gamma = 1.4$ for the air. Figure 5.6 illustrates the sketch for the boundary condition setup for the single mesh and overset mesh cases.

Initially, the imposed boundary conditions considered a subsonic or supersonic inlet - depending on the normal face velocity - forcing the free-stream Mach at the entrance, an outlet at the exit forcing $p = \frac{1}{\gamma}$ for subsonic and internal solution extrapolation for supersonic, and a slip wall condition at the cylinder. The initial solution in the fluid domain is imposed as the free stream conservative properties. However, despite the fact that the outer boundary is defined at a 100-cylinder radius away from the body, a residue wave stayed in the domain initiated at the first step due to the abrupt initial solution imposed around the cylinder, where the normal velocity component is zero and the fluid domain properties are the free stream values. Therefore, the farfield boundary conditions had to be modified in order to impose a non-reflective farfield and, hence, overcome the difficulty described, as sketched in Fig. 5.6. For the overset case, the cells around the external boundary of the near-body mesh are marked as an overset region during the mesh generation. These overset flags are used in the receptor-donor connectivity procedure to establish how the data is interpolated from one mesh to the other at each time step.

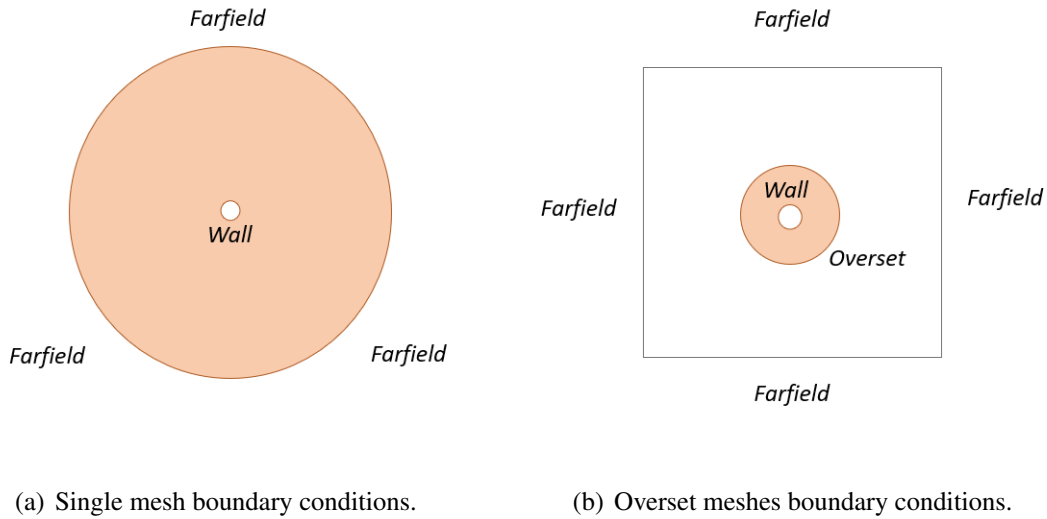


FIGURE 5.6 – Inviscid cylinder boundary conditions sketch for single mesh (left) and overset mesh (right) cases.

The meshes generated for the present tests considered a mesh with 20×32 cells for the single mesh case, two background meshes, a 32×32 and a 24×24 cells, and a near-body mesh with 20×20 cells as illustrated in Fig. 5.7. The 24×24 background mesh illustrated in Fig. 5.7(e) has a refinement at the central horizontal and vertical lines that crosses the cylinder center. The reason for this refinement is due to difficulties in edge cases for the cells at the overset region. Occasionally, a fringe cell flux point, that requires interpolated data, may not be embedded by a donor cell. Moreover, since its neighbor cell is deactivated, *i.e.*, it is a hole cell, no flux is defined in this interface during the simulation making the solution to diverge. Hence, the length scale around the overset region between the background and near-body mesh needs to be similar so that the receptor-donor relationship can be fully established altogether with the existence of the fringe circuit which limits the BFS hole propagation.

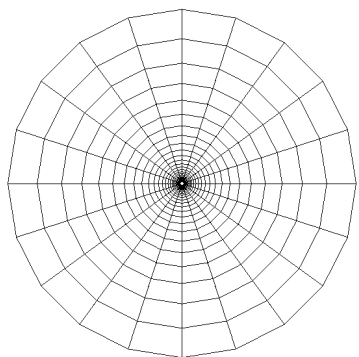
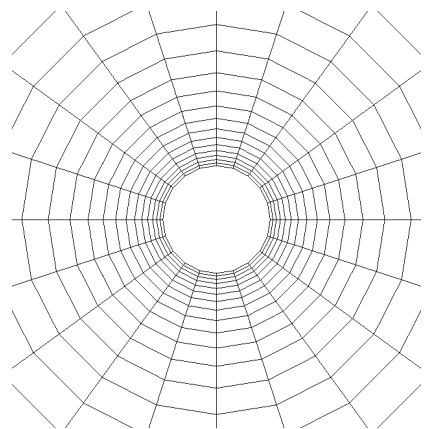
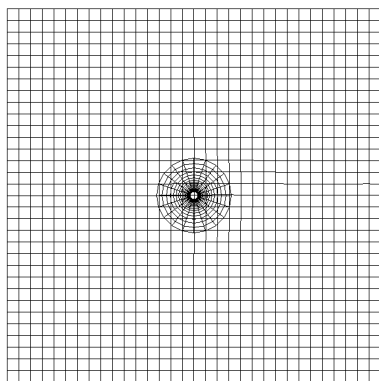
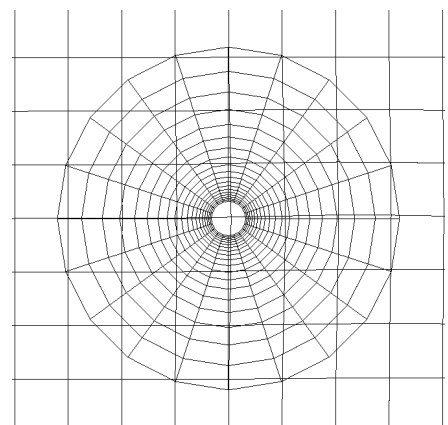
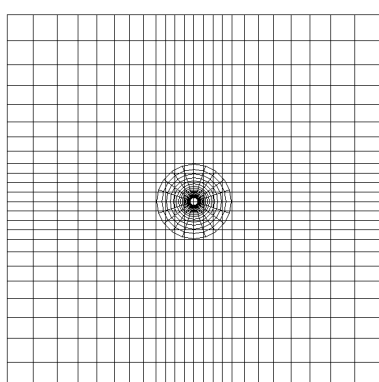
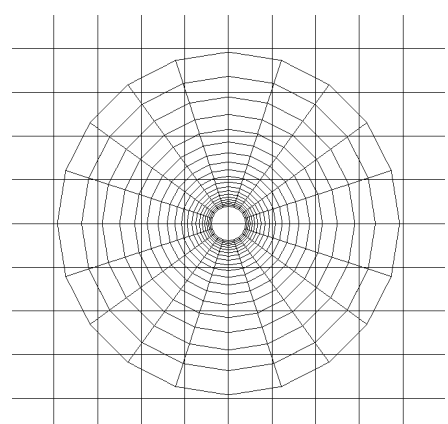
(a) 20×32 - single mesh view.(b) 20×32 - single mesh close-up view.(c) 32×32 background and 20×20 near-body mesh view.(d) 32×32 background and 20×20 near-body mesh close-up view.(e) 24×24 background and 20×20 near-body mesh view.(f) 24×24 background and 20×20 near-body mesh close-up view.

FIGURE 5.7 – Cylinder single and overset meshes with 1:100 cylinder radius ratio.

Two different scenarios are tested over the inviscid cylinder test case: a low-order case with P2Q1 and a high-order case with P5Q4 resolution. Figure 5.8 shows the close-up views of the Spectral Difference meshes around the cylinder walls obtained from the aforementioned grids. The grid length scale around the cylinder is imposed to be similar between the single and near-body meshes so that the number of degrees of freedom can be comparable. Although, the effect of curvature is not visually noticeable for the P5Q4 linear visualization of the grid points in Figs. 5.8(c) and 5.8(d), the position of the flux-points and the entire standard space projection is affected through the high-order Jacobian representation over a high-order cell.

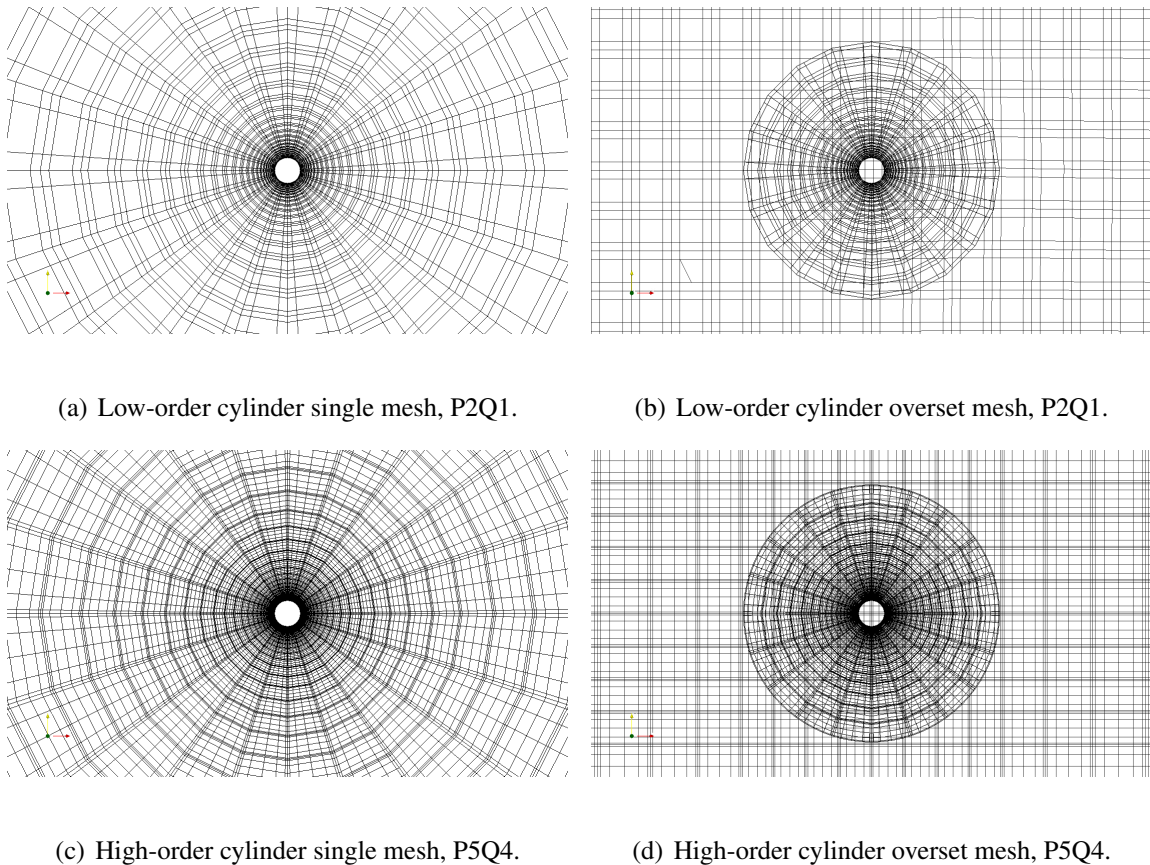


FIGURE 5.8 – Close-up views of the cylinder single and overset Spectral Difference meshes for two different scenarios of mesh and solver orders: P2Q1 and P5Q4.

For the overset grid runs, the receptor-donor connectivity outputs special cell tags at a pre-processing stage to identify the fringe and hole cells. Figures 5.9(a) and 5.9(c) illustrate the

background cell tags which are defined as 0 to represent a fluid (blue), 1 for hole cells (red), and 2 for fringe cells (light-gray). Note that the fringe cells in gray formed the fringe-circuit in which the hole cells lay inside with no fluid cell as neighbor. This step is mandatory for the presented methodology due to the assumptions of the hole cell propagating procedure to establish the connectivity. These gray cells are used as donor-receptor interface where the solution transits between the near-body and background meshes. Moreover, in contrast to the background fringe cells, as illustrated in Figs. 5.9(b) and 5.9(d), the near-body fringe cells are used solely as donors to the ghost flux points at the inner boundary of the background fringe circuit.

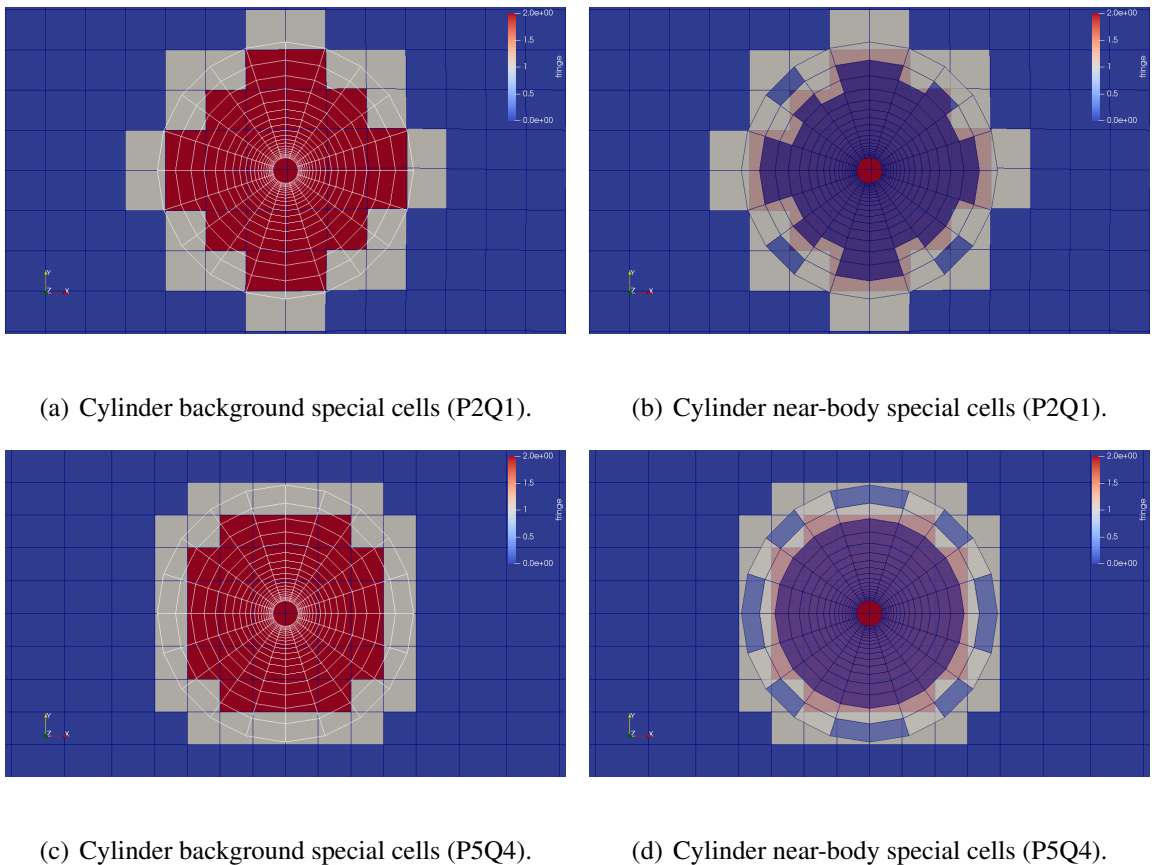


FIGURE 5.9 – Cylinder overset grid special cells for the background (left) and near-body meshes (right). Fringes in light-gray, holes in red, and fluid cells in blue.

The results of residue are shown in Fig. 5.10 where the y-axis is the L2-norm order of magnitude of the entire residue vector including all conservative property residue and the x-

axis is the number of time iterations. The single mesh results are represented by the mesh size in the legend through the suffix 20×32 , while the overset mesh for low-order is $20 \times 20_32 \times 32$ and high-order, $20 \times 20_24 \times 24$. The rate of change of the residue magnitude for the single mesh results is similar for both single mesh test cases, both reaching around 10^{-7} of residue L2-norm in 10^5 iterations. However, a significant difference can be seen when comparing the behavior of the residue for the overset tests. The low-order (P2Q1) overset case reached a $10^{-7.5}$ residue L2-norm in approximately 50,000 iterations.

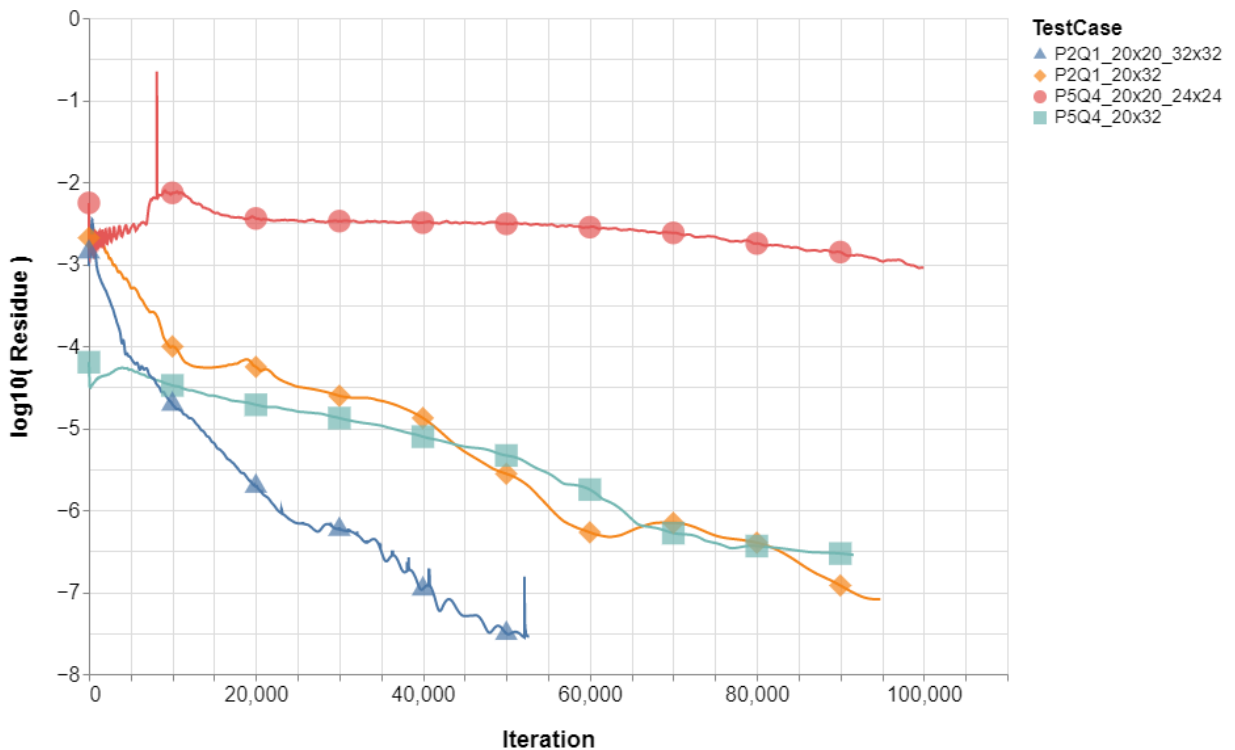


FIGURE 5.10 – Comparison of the L2-norm of the density residue for the single and overset cases with different mesh and solver orders.

In contrast, the residue for the high-order (P5Q4) overset case only reached around 10^{-3} residue L2-norm at the end of the 10^5 iterations. In fact, by observing the solution throughout the iterations, what has increased its norm is a residue wave that starts at the cylinder wall and propagates up to the outer boundary of the both background and single meshes, where the non-

reflective boundary condition allows such wave to exit the computational domain. Nonetheless, due to the small time step, as a result of a higher P , and small characteristic length, the number of iterations needed so that this residue wave reaches the outer boundary is very large. The criterion used here to stop the iterations for this scenario was, then, to wait until the residue wave is totally transported from the near-body mesh to a considerable distance out of the fringe circuit of the background mesh. Over this consideration, the residue around the near-body mesh for the high-order overset plunges to 10^{-7} .

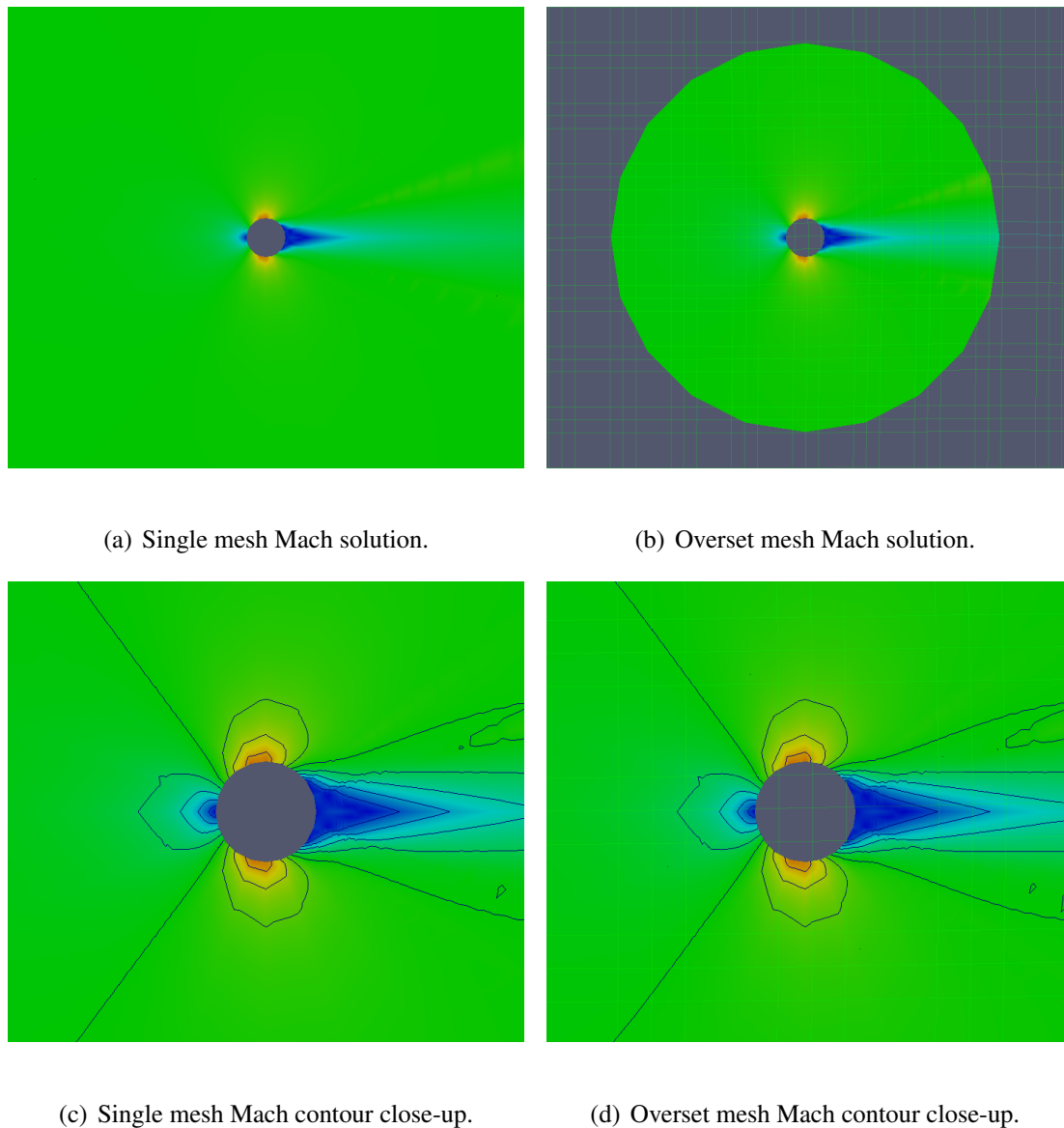


FIGURE 5.11 – Cylinder single and overset grid solution in terms of Mach number contours for P2Q1.

The solution for both single and overset cases converged around 10^{-7} of residue magnitude and the Mach number solution is, then, obtained and illustrated in Figs. 5.11 and 5.12. The Mach number contours are shown with a fixed colormap ranging from 0.0 to 0.4 and step 0.02 in Figs. 5.11(c), 5.11(d), 5.12(c) and 5.12(d). For the overset scenarios, the background mesh is presented by the solution wireframe colored by the Mach number while the near-body mesh follows the aforementioned colormap over its solution surface. The reason is to ease the visualization since the data of interest for this test case lies entirely in the near-body mesh. Thus, the background mesh solution here does not provide any additional information.

The behavior of the solution comparing the single and overset results are nearly identical. In the low-order cases, for both single and overset meshes, even though the solution is 3rd order, i.e., $P = 2$, due to the inadequate geometrical representation of the cylinder curvature, a non-physical solution at the cylinder trailing edge is formed which can be observed in Fig. 5.11. For the high-order cases, instead, the expected solution double symmetry for the inviscid cylinder is presented, as shown in Figs. 5.12(c) and 5.12(d).

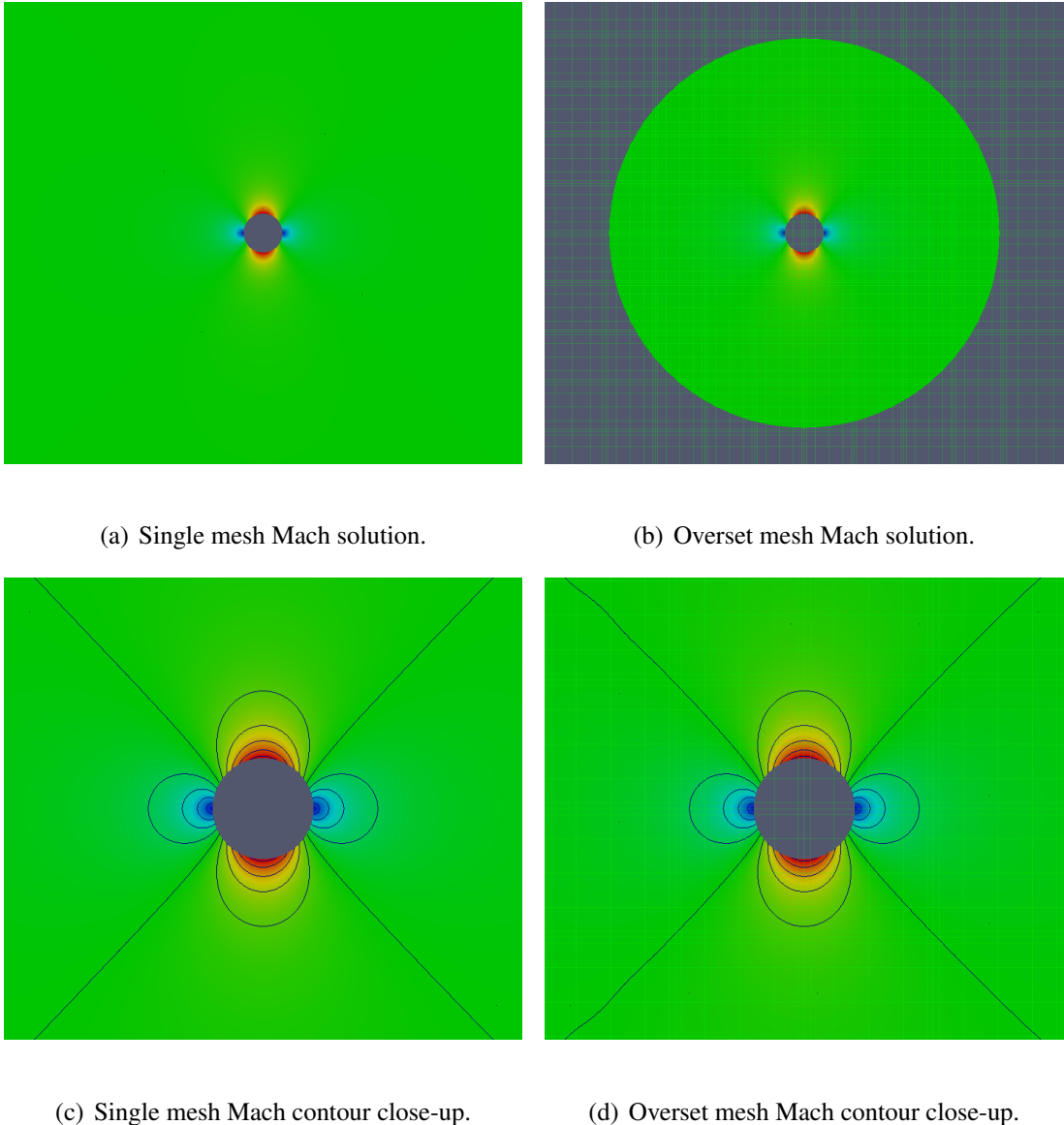


FIGURE 5.12 – Cylinder single and overset grid solution in terms of Mach number contours for P5Q4.

5.3 Isentropic Vortex

The 2-D inviscid isentropic vortex problem is chosen to benchmark the single and overset numerical solutions. Due to the presence of an analytical solution, it is commonly used in the literature to test the accuracy of an Euler simulation [37] and, in particular, for high-order methods as a validation test case of the International Workshop on High-Order Methods in CFD

[36] and in several articles [38, 29, 9].

The mean flow properties considered to be the freestream u_∞ and v_∞ as the velocity components, ρ_∞ as density, p_∞ as pressure, T_∞ as temperature, with the values ($u_\infty=1$, $v_\infty=1$, $\rho_\infty=1$, $p_\infty=1$, $T_\infty=1$). The mean flow velocity components here define how the vortex is transported. The vortex center position, (x_c, y_c) , can be determined at any time t by $x_0+u_\infty t$ and $y_0+v_\infty t$ and $(x_0=0, y_0=0)$ is the initial coordinates of the vortex center. The initial condition for the single and overset tests is the analytical solution for the inviscid isentropic vortex with no perturbation in entropy ($\delta S = 0$) for the mean flow field. The perturbations in velocity and temperature can be given by

$$\delta u = -\frac{\Delta y \beta}{2\pi} e^{\frac{1-r^2}{2}}, \delta v = \frac{\Delta x \beta}{2\pi} e^{\frac{1-r^2}{2}}, \quad (5.5)$$

$$\delta T = -\frac{(\gamma - 1)\beta}{8\gamma\pi} e^{1-r^2} \quad (5.6)$$

where δu and δv are, respectively, the perturbations of the velocity in x and y direction and δT is the perturbation in the fluid temperature. The β parameter is the vortex strength, the coordinates $(\Delta x, \Delta y) = (x - x_0, y - y_0)$, and $r^2 = (\Delta x^2 + \Delta y^2)$. The fluid is assumed as a perfect gas with $\gamma=1.4$ for air. From the isentropic relations, the conservative fluid properties $\rho = \rho_\infty + \delta\rho$, $u = u_\infty + \delta u$, $v = v_\infty + \delta v$, $T = T_\infty + \delta T$ can be determined by

$$\rho = T^{\frac{1}{\gamma-1}} = (T_\infty + \delta T)^{\frac{1}{\gamma-1}}, \quad (5.7)$$

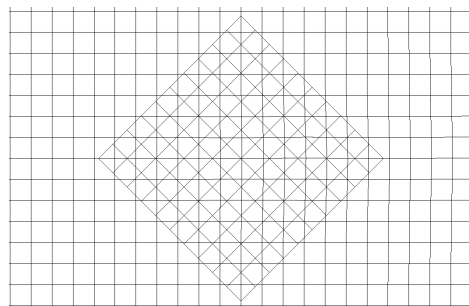
$$\rho u = \rho(u_\infty + \delta u), \quad (5.8)$$

$$\rho v = \rho(v_\infty + \delta v), \quad (5.9)$$

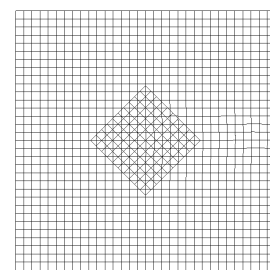
$$p = \rho^\gamma, \quad (5.10)$$

$$E = \frac{p}{\gamma - 1} + \frac{1}{2} \rho [(u_\infty + \delta u)^2 + (v_\infty + \delta v)^2]. \quad (5.11)$$

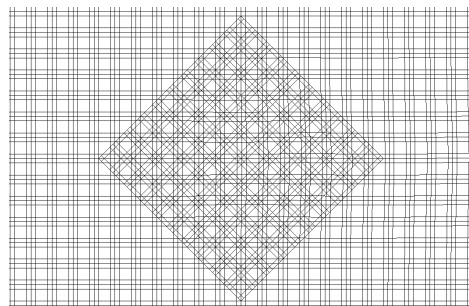
The boundary conditions used for the overset test case over the isentropic vortex problem are a non-reflective farfield at the outer boundary of the background mesh and an overset boundary condition at the near-body mesh outer boundary. This is imposed at the mesh generation stage. In the present work, the open source GMSH software is used for this matter [39]. Several scenarios are tested for this problem combining three different meshes with 16×16 , 32×32 , and 64×64 cells for the background mesh and, respectively, 5×5 , 10×10 , and 20×20 near-body mesh. For single mesh cases, the background meshes are used. For instance, Figs. 5.13(a) and 5.13(b) show a 32×32 cell background mesh and a 10×10 cell near-body mesh. The latter is rotated 45 degrees so that its right outer boundary face is aligned with the vortex velocity. The tests provided for this problem included several different orders of accuracy of the Spectral Difference method, ranging from $P = 2$ to $P = 6$. Figure 5.13 illustrates the 32×32 background and 10×10 near-body meshes for the Spectral Difference method with orders ranging from $P = 2$ to $P = 4$.



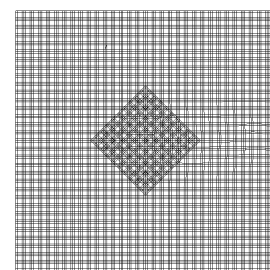
(a) Close-up snapshot of the overset mesh.



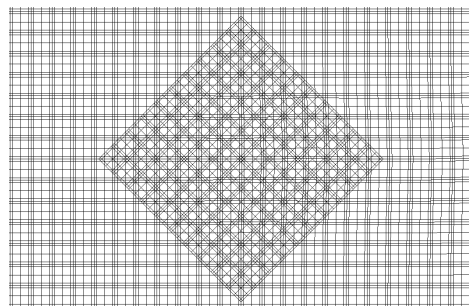
(b) Overset mesh.



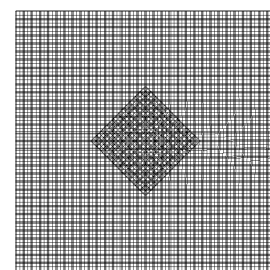
(c) P=2 close-up view.



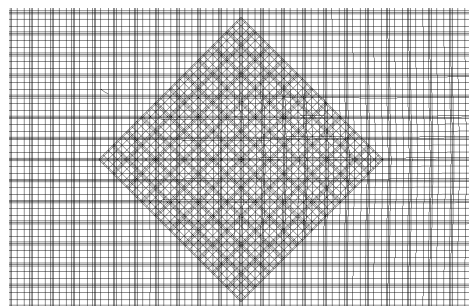
(d) P=2 overall view.



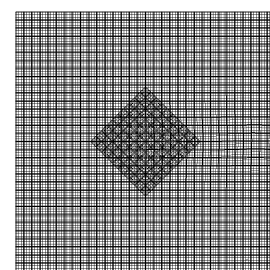
(e) P=3 close-up view.



(f) P=3 overall view.



(g) P=4 close-up view



(h) P=4 overall view.

FIGURE 5.13 – Spectral Difference mesh for the 32×32 background and 10×10 near-body mesh case.

The initial solution is given by the analytical solution described in Eqs. 5.7, 5.8, 5.9, 5.11 and the initial solution for the density contours can be seen in Fig. 5.14. Note that the setup of the near-body mesh is precisely built so that the entire vortex fits inside the near-body mesh in the initial solution. Figure 5.14(a) shows the initial density solution at background mesh where the hole cells can be seen fully overlapped by the near-body mesh. Figure 5.14(b) shows the near-body mesh initial density solution. Figure 5.14(c) shows the overall overset initial density solution for both background and near-body mesh.

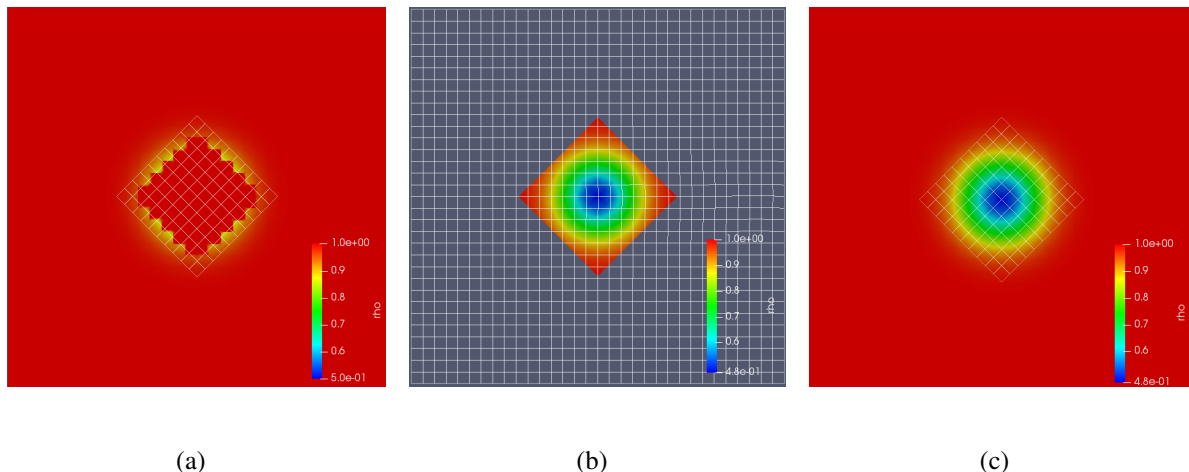


FIGURE 5.14 – Initial solution for the density in the overset setup.

Figure 5.15 presents the background and near-body mesh special cell tags. The fringe cells are represented here in light-blue color, hole cells in light-orange and the reactivated hole cells in red. Note that for the near-body fringes, since only the inward background fringe circuit receives data from the near-body mesh, the addition of flux-points in the background cells due to higher P values increases the number of near-body fringes. In all scenarios, the fringe circuit is formed as can be seen in Figs. 5.15(a), 5.15(c), and 5.15(e).

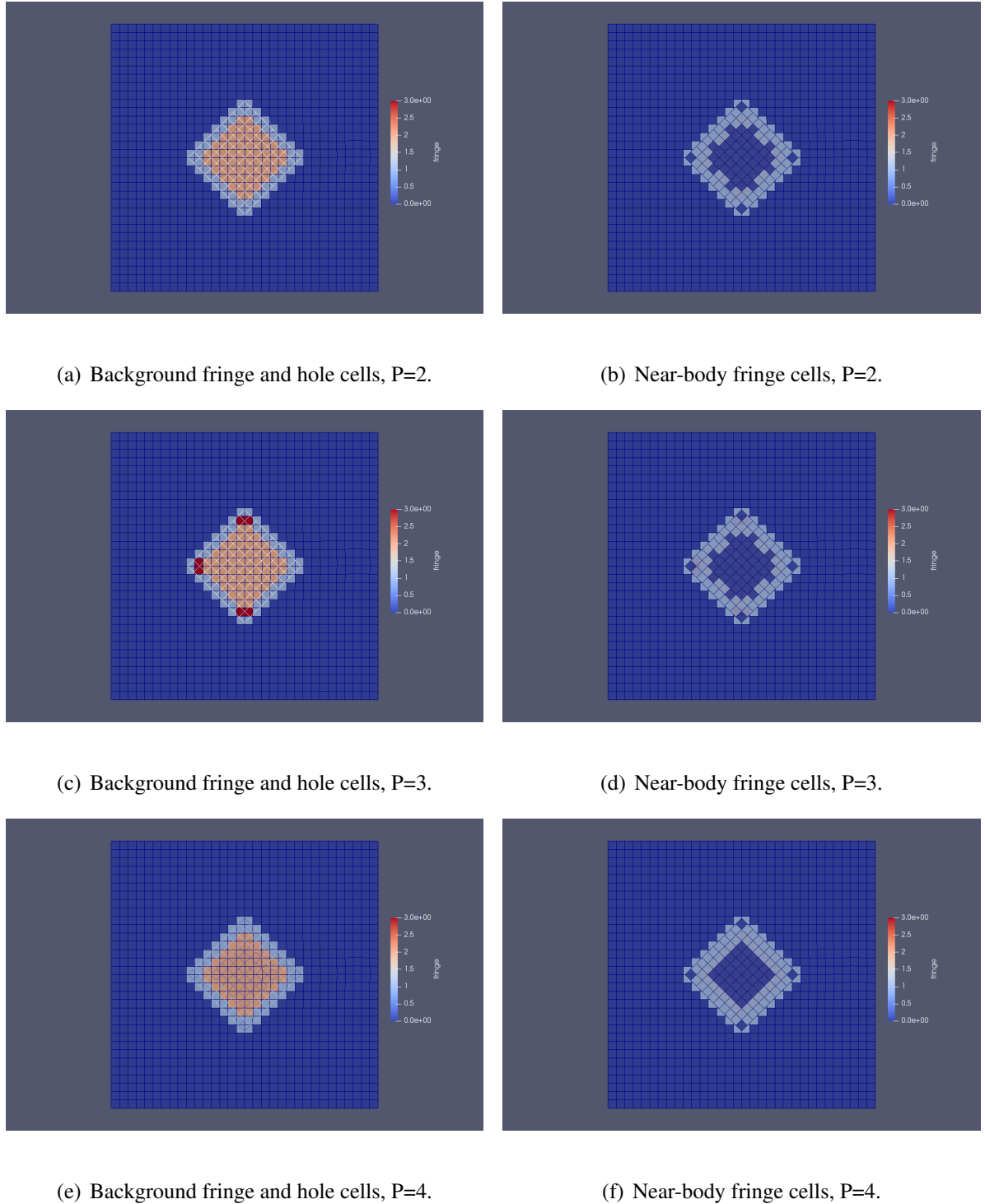


FIGURE 5.15 – Fringe and hole cells for different orders of accuracy of the Spectral Difference method in the overset vortex case.

A special edge case is addressed in this test when a flux-point located at the fringe-circuit interface is not overlapped by the near-body mesh. As illustrated in Fig. 5.16, the green orange

dots represent interface flux points of some background fringe cells. The white wireframe is the near-body mesh, and as it can be seen, the green dots lay outside of the near-body outer boundary. Therefore, no receptor-donor connectivity can be established since the interpolation is only defined within a cell domain. The proposed solution for this issue is to reactivate the hole cells represented in red that own flux points with no near-body cell overlapping. The reactivation restores the unstructured cell connectivity between the reactivated cell and its fringe cell neighbors and tag this hole cell as a fringe cell. Then, the reactivated cell becomes part of the fringe circuit and its flux points interfaces are searchable to establish additional receptor-donor connectivity.

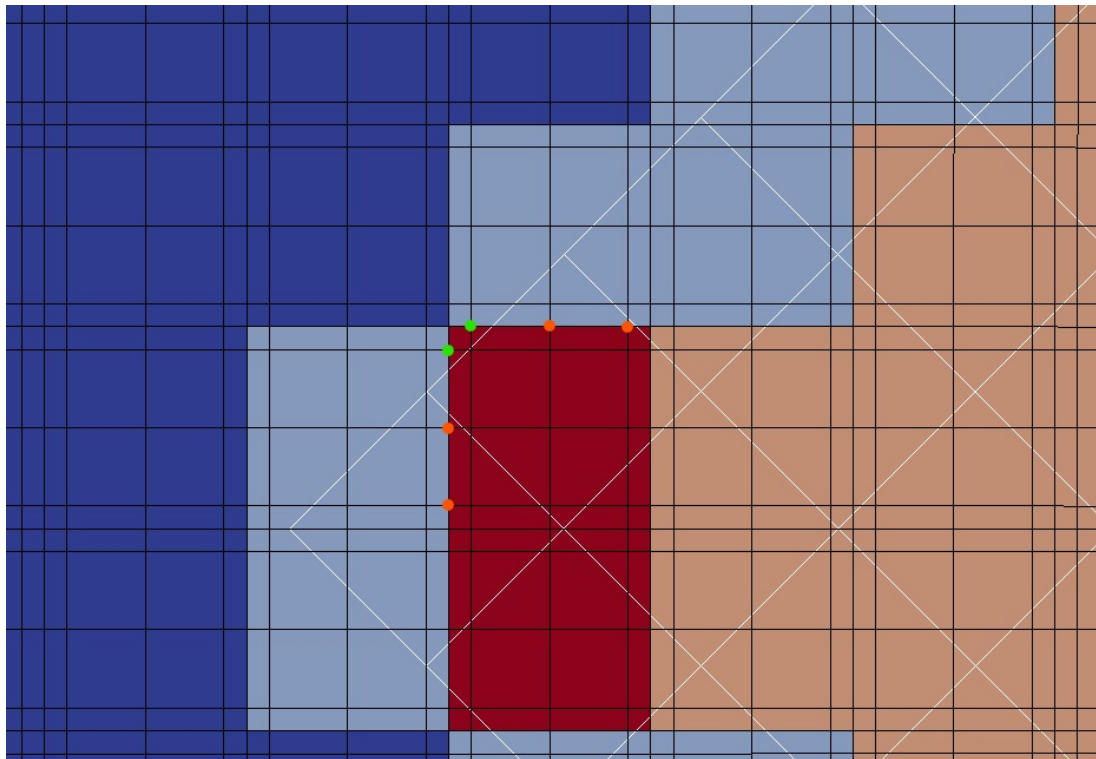


FIGURE 5.16 – Special case when a flux-point of a fringe cell is out of the near-body mesh (green dots). Background fringe cells in light blue, hole cells in light orange and the special case of fringe cells in red.

The solution in terms of density contours for the selected mesh of 32×32 background and 10×10 near-body meshes can be seen in Fig. 5.17. The density contours are presented through

a colormap ranging from 0.5 to 1.0 and three time periods are chosen to present the solution: $t = 0$ (initial solution), $t = 20$, and $t = 50$. The time here is normalized so that the $t = 100$ would indicate the time at which the vortex center is located at the upper-right edge in the background mesh. Additionally, Figure 5.17 shows the results for different orders of accuracy of the Spectral Difference method from $P = 2$ to $P = 4$. The numerical solution at $t = 20$ represents the simulation time where half of the vortex is in the near-body mesh and the other half in the background mesh, as demonstrated in Figs. 5.17(b), 5.17(e), and 5.17(h). For $t = 50$ the vortex is completely transported to the background mesh with its magnitude and symmetry preserved for both setups.

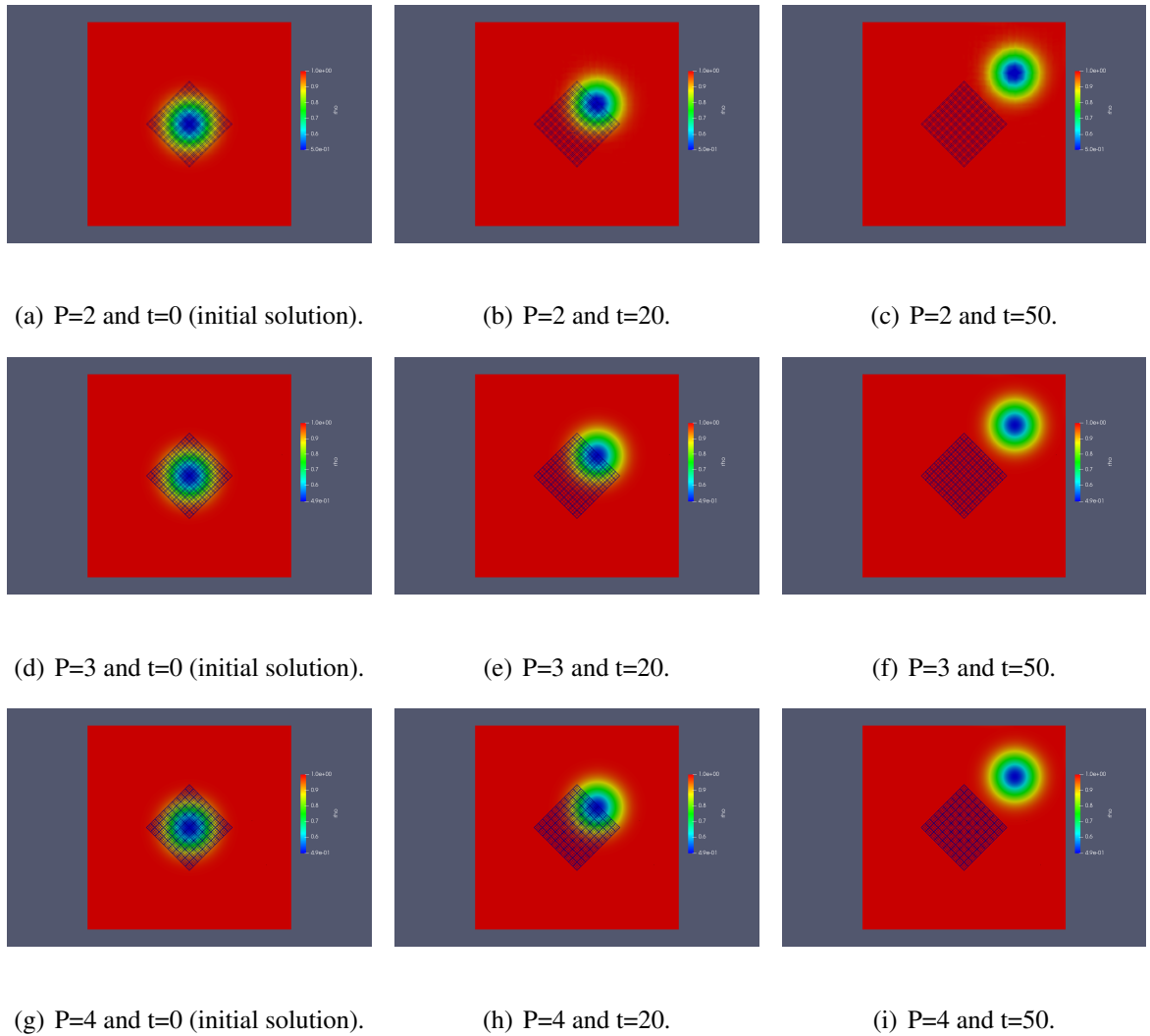


FIGURE 5.17 – Numerical density contours for the solution of the vortex overset case with $P=4$ after different time periods.

In order to measure the accuracy of the presented overset methodology, since the isentropic vortex problem presents an analytical solution and an isentropic property, the L2-norm of the entropy error is used. Several scenarios are simulated including different orders of accuracy of the Spectral Difference method and different mesh refinements for both single and overset mesh. The single mesh tests are done by using the background mesh only. Figure 5.18 demonstrates the results obtained for these runs. The y-axis is the L2-norm of the entropy error and the x-axis represents the Spectral Difference method polynomial order, *i.e.*, P . The dashed lines are the

results for the single mesh cases, while the solid lines represent the overset mesh cases. For a given mesh refinement, by increasing the solver order, the entropy error magnitude decays in a nearly linear rate, in the log scale, reaching low entropy errors.

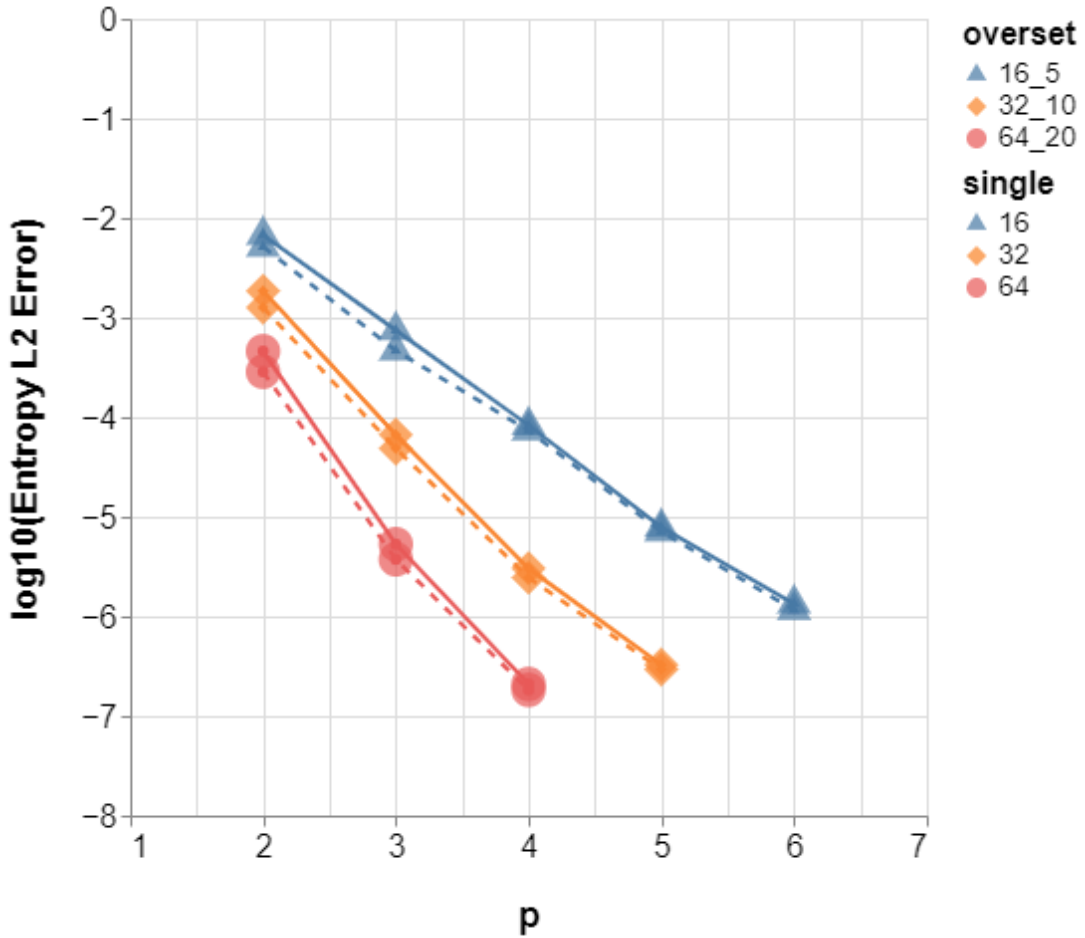


FIGURE 5.18 – Comparison of the L2-norm of the entropy error for the single and overset cases with different values for P and mesh size.

TABLE 5.1 – Values of the median CPU time per iteration in milliseconds.

p	Single			Overset		
	16x16	32x32	64x64	16x16_5x5	32x32_10x10	64x64_20x20
2	17	76	304	15	63	264
3	34	153	602	31	127	510
4	66	278	1132	59	241	945
5	129	503	-	113	436	-
6	217	-	-	200	-	-

Table 5.1 shows results of the median CPU time per numerical iteration for the same range

of P and mesh size. The CPU time results show that the current implementation of the overset code have presented a lower median CPU time per iteration in all experiments in comparison with the single mesh cases. Since the overset residue calculation is solved asynchronously for both meshes in the overset setup, the additional time cost due to the overset data communication are being compensated by the parallel residue calculation of the overset meshes. Note that the parallelism here is only over the meshes, not the cells. The residue is still calculated sequentially per cell in both single and overset cases.

6 Conclusion

6.1 Concluding Remarks

In the present work, a high-order solver coupled with a conservative high-order face-based interpolation approach for overset grids is implemented and its main aspects are addressed. The physical phenomena are represented by the 2-D Euler equations numerically discretized with an arbitrarily high-order polynomial-based Spectral Difference method. High-order meshes are considered in the solver and used to improve the receptor-donor connectivity by leveraging high-order nodes at the curved cell interfaces. A 3rd-order Strong-Stability-Preserving Runge-Kutta method with 3 stages is used as explicit time-marching approach in the present effort, showing satisfactory residue convergence.

The solver has been successfully validated through the tests for both low and high order achieving the expected results, as indicated in the literature. The overset results obtained have demonstrated the capability of the kd-tree for the geometric searching problem as well as the face-based interpolation approach as candidate to preserve the solution order of accuracy and conservation. The mesh generation for the overset cases has been demonstrated as a crucial procedure to achieve the presented results, once several edge cases can appear around the overset

region. In particular, for high-order curved meshes, not all of the inward fringe-circuit flux-points lay inside of the near-body mesh domain. Therefore, the flux can not be reconstructed in these scenarios and an alternative additional step is proposed to overcome this issue, adding robustness to the presented solver by reactivating specific hole cells at the fringe-circuit.

Furthermore, the methodology for the high-order overset grid solver presented satisfactory results over the inviscid cylinder and isentropic vortex test cases. In the cylinder case, the expected double symmetry solution, for instance, for the Mach number contours, around the cylinder wall is achieved when the cylinder curvature is represented by the high-order mesh. Moreover, for the isentropic vortex, not only the presented solution fully transported the vortex from the near-body mesh to the background mesh, but also effectively preserved the vortex symmetry and magnitude with an adequate order of magnitude for the L2-norm entropy error, when compared to the literature.

The CPU performance tests show satisfactory results comparing the single and overset vortex cases presenting similar median values of CPU time per iteration for different solver orders and mesh sizes. The reason is due to the asynchronously calculation of the residue over the overset meshes implemented in the present code which overcomes the additional time cost of the overset steps.

6.2 Future Work

In Unsteady Aerodynamics applications, several numerical experiments consider moving boundaries to address the physical representation of movable objects inside the fluid domain. The present work discusses and presents results over a state-of-the-art methodology for overset grids with high-order conservative interpolation applied to some validation controlled applications. Apart from the initially intended investigation, additional aspects can be addressed for future research.

As demonstrated throughout the present effort, the overset grid conservative interpolation methodology has shown interesting results for unstructured and curved meshes. In this scenario, difficulties can arise in the imposition of periodic boundary conditions depending on the outer boundary geometry in unstructured grids. In general, a periodic boundary is forced to establish a 1:1 cell and interface point relation between two far apart boundaries. The implementation of this type of boundary condition can bring considerable complexity for unstructured grid solvers. On the other hand, there are several applications in which the use of periodic boundary conditions would be extremely useful, especially for reducing the computational requirements. Nonetheless, an overset grid coupled with a conservative high-order interpolation can be a suitable candidate for the periodic boundary condition due to its flexibility and accurate data communication.

Furthermore, the capability to provide a suitable representation of strong discontinuities in the simulation is extremely relevant for several aerospace applications. Commonly, the use of limiter formulation addresses local test markers to identify discontinuities in the simulation. For

some limiters, the information around the vicinity of a cell is necessary to build the local test, which at an overset region can be challenging. Therefore, a representation of discontinuities could be a possible extension of the use of the present methodology by investigating how to couple limiter formulations with the present data communication approach.

Bibliography

- [1] Hirsch, C., *Numerical Computation of Internal and External Flows, Volume 2: Computational Methods for Inviscid and Viscous Flows*, Wiley, New York, 1991. xvii, 31, 36, 37
- [2] Rockwell, D., “Vortex-Body Interactions,” *Annual Review of Fluid Mechanics*, Vol. 30, No. 1, 1998, pp. 199–229. 26
- [3] Abras, J., Lynch, C., and Smith, M., “Advances in Rotorcraft Simulations with Unstructured CFD,” *Annual Forum Proceedings - AHS International*, Vol. 3, 01 2007. 26
- [4] Costes, M., Renaud, T., and Rodriguez, B., “Rotorcraft Simulations: A Challenge for CFD,” *International Journal of Computational Fluid Dynamics*, Vol. 26, No. 6-8, 2012, pp. 383–405. 26
- [5] Powell, K. G., Roe, P. L., and Quirk, J., “Adaptive-Mesh Algorithms for Computational Fluid Dynamics,” *Algorithmic Trends in Computational Fluid Dynamics*, edited by M. Y. Hussaini, A. Kumar, and M. D. Salas, Springer New York, New York, NY, 1993, pp. 303–337. 27
- [6] Persson, P., Edelman, A., and Strang, G., “Mesh Generation for Implicit Geometries,” 2005. 27
- [7] Galbraith, M. C., *A Discontinuous Galerkin Chimera Overset Solver*, Ph.D. thesis, Doctor Program in Aerospace Engineering, University of Cincinnati, Cincinnati, OH, 2013. 27, 62, 63
- [8] Crabil, J., Witherden, F., and Jameson, A., “A Parallel Direct Cut Algorithm for High-Order Overset Methods with Application to a Spinning Golf Ball,” *Journal of Computational Physics*, Vol. 374, 2018, pp. 692–723. 27
- [9] Duan, Z., *A High-Order Flux Reconstruction Method for Dynamic Moving Grids*, Ph.D. thesis, Doctor Program in Aerospace Engineering, University of Kansas, Lawrence, KS, 2019. 27, 52, 63, 84
- [10] Duan, Z. and Wang, Z. J., “High-Order Overset Flux Reconstruction Method for Dynamic Moving Grids,” *AIAA Journal*, Vol. 58, No. 10, 2020, pp. 4534–4547. 27
- [11] Rogers, S. E., Suhs, N. E., and Dietz, W. E., “PEGASUS 5: An Automated Preprocessor for Overset-Grid Computational Fluid Dynamics,” *AIAA Journal*, Vol. 41, No. 6, 2003, pp. 1037–1045. 28, 62

- [12] Sankaran, V., Wissink, A., Datta, A., Sitaraman, J., Jayaraman, B., Potsdam, M., Katz, A., Kamkar, S., Roget, B., Mavriplis, D., Saberi, H., Chen, W.-B., Johnson, W., and Strawn, R., “Overview of the Helios Version 2.0 Computational Platform for Rotorcraft Simulations,” *AIAA Journal*, 01 2011. [28](#)
- [13] Liu, Y., Vinokur, M., and Wang, Z. J., “Spectral Difference Method for Unstructured Grids I: Basic Formulation,” *Journal of Computational Physics*, Vol. 216, 2006, pp. 780–801. [28](#), [40](#)
- [14] Wang, Z. J., Liu, Y., May, G., and Jameson, A., “Spectral Difference Method for Unstructured Grids II: Extension to the Euler Equations,” *Journal of Scientific Computing*, Vol. 32, No. 1, July 2007, pp. 3938–3956. [28](#), [40](#), [41](#)
- [15] May, G. and Jameson, A., “A Spectral Difference Method for the Euler and Navier-Stokes Equations on Unstructured Meshes,” AIAA Paper No. 2006-0304, *Proceedings of the 44th AIAA Aerospace Sciences Meeting*, Reno, NV, Jan. 2006. [28](#), [40](#), [41](#)
- [16] van den Abeele, K., *Development of High-Order Accurate Schemes for Unstructured Grids*, Ph.D. thesis, Doctor Program in Mechanical Engineering, Vrije Universiteit Brussel, Brussels, Belgium, 2009. [28](#), [40](#), [43](#)
- [17] Moreira, F. M., *A Study of High-Order Unstructured Spectral Difference Schemes for Compressible Flows*, Master’s thesis, Graduate Program in Space Science and Technology, Instituto Tecnológico de Aeronáutica, São José dos Campos, Brasil, 2016. [28](#), [40](#), [41](#)
- [18] Gao, H. and Wang, Z., “A Conservative Correction Procedure via Reconstruction Formulation with the Chain-Rule Divergence Evaluation,” *Journal of Computational Physics*, Vol. 232, 01 2013, pp. 7?13. [28](#)
- [19] Aguiar, A. R. B., *Study of Viscous Flows Using High-Order Methods and Curved Boundary Treatment*, Master’s thesis, Graduate Program in Space Science and Technology, Instituto Tecnológico de Aeronáutica, São José dos Campos, Brasil, 2018. [28](#)
- [20] Sun, Y., Wang, Z., and Liu, Y., “High-Order Multidomain Spectral Difference Method for the Navier-Stokes Equations on Unstructured Hexahedral Grids,” *Communications in Computational Physics Commun. Comput. Phys.*, Vol. 2, 05 2007, pp. 310–333. [43](#)
- [21] Roe, P., “Approximate Riemann Solvers, Parameter Vectors, and Difference Schemes,” *Journal of Computational Physics*, Vol. 43, No. 2, 1981, pp. 357?372. [44](#)
- [22] Harten, A. and Hyman, J. M., “Self Adjusting Grid Methods for One-Dimensional Hyperbolic Conservation Laws,” *Journal of Computational Physics*, Vol. 50, No. 2, 1983, pp. 235–269. [47](#)
- [23] Blazek, J., *Computational Fluid Dynamics: Principles and Applications*, Elsevier, Oxford, UK, 2001. [47](#)
- [24] Chen, R. and Wang, Z., “Fast, Block Lower-Upper Symmetric Gauss-Seidel Scheme for Arbitrary Grids,” *Aiaa Journal - AIAA J*, Vol. 38, 12 2000, pp. 2238–2245. [49](#)

- [25] Gottlieb, S., Grant, Z. J., and Isherwood, L., “Strong Stability Preserving Integrating Factor Runge-Kutta Methods,” *SIAM Journal on Numerical Analysis*, Vol. 56, No. 6, 2018, pp. 3276?3307. [49](#)
- [26] Ruuth, S., Spiteri, R., and Ruuth, J., “A New Class of Optimal High-Order Strong-Stability-Preserving Time Discretization Methods,” *SIAM J. Numer. Anal.*, Vol. 40, 02 2002. [49](#)
- [27] Duan, Z. and Wang, Z. J., “High Order FR/CPR Method for Overset Meshes,” *23rd AIAA Computational Fluid Dynamics Conference – AIAA Aviation Forum*, AIAA Paper No. 2017-3094, Denver, CO, 2017. [52](#), [53](#)
- [28] Duan, Z. and Wang, Z. J., “A High Order Overset FR/CPR Method for Dynamic Moving Grids,” 2019. [52](#), [63](#)
- [29] Crabil, J. A., Sitaraman, J., and Jameson, A., “A High-Order Overset Method on Moving and Deforming Grids,” *AIAA Modeling and Simulation Technologies Conference*, 2016. [52](#), [53](#), [84](#)
- [30] Bentley, J. L., “Multidimensional Binary Search Trees Used for Associative Searching,” *Communications of the ACM*, Vol. 18, No. 69, 1975, pp. 509?517. [55](#)
- [31] Skrodzki, M., “The k-D Tree Data Structure and a Proof for Neighborhood Computation in Expected Logarithmic Time,” 2019. [55](#)
- [32] Cormen, T. H., Leiserson, C. E., Rivest, R. L., and Stein, C., *Introduction to Algorithms*, Third Edition, The MIT Press, 3rd ed., 2009. [61](#)
- [33] Nastase, C., Mavriplis, D., and Sitaraman, J., “An Overset Unstructured Mesh Discontinuous Galerkin Approach for Aerodynamic Problems,” *49th AIAA Aerospace Sciences Meeting including the New Horizons Forum and Aerospace Exposition*, 2016. [62](#)
- [34] Brazell, M. J., Sitaraman, J., and Mavriplis, D. J., “An Overset Mesh Approach for 3D Mixed Element High Order Discretizations,” *Journal of Computational Physics*, Vol. 322, No. 10, 2016, pp. 33–51. [62](#)
- [35] Shapiro, A. H., *The Dynamics and Thermodynamics of Compressible Fluid Flow*, Wiley, New York, 1953. [68](#)
- [36] Wang, Z. J., Cagnone, J. S., Careni, D., de Wiart, C. C., Couaillier, V., Fidkowski, C., Galbraith, M., Hartman, R., Gooch, C. O., Persson, P.-O., Hillewaert, K., Ekaterinaris, J., Huynh, H. T., Kroll, N., and Vincent, P., “HiOCFD4 4th International Workshop on High-Order CFD Methods,” <https://how4.cenaero.be>, 2015. [69](#), [84](#)
- [37] Yee, H., Sandham, N., and Djomehri, M., “Low-Dissipative High-Order Shock-Capturing Methods Using Characteristic-Based Filters,” *Journal of Computational Physics*, Vol. 150, No. 1, 1999, pp. 199–238. [83](#)
- [38] Huynh, H., Wang, Z., and Vincent, P., “High-Order Methods for Computational Fluid Dynamics: A Brief Review of Compact Differential Formulations on Unstructured Grids,” *Computers & Fluids*, Vol. 98, 2014, pp. 209–220, 12th USNCCM Mini-Symposium of High-Order Methods for Computational Fluid Dynamics - A Special Issue Dedicated to the 80th Birthday of Professor Antony Jameson. [84](#)

- [39] Geuzaine, C. and Remacle, J.-F., “Gmsh: A 3-D Finite Element Mesh Generator with built-in Pre- and Post-Processing Facilities,” *International Journal for Numerical Methods in Engineering*, Vol. 79, No. 11, 2009, pp. 1309–1331. [85](#)

FOLHA DE REGISTRO DO DOCUMENTO			
1. CLASSIFICAÇÃO/TIPO DM	2. DATA 28 de setembro de 2022	3. REGISTRO N° DCTA/ITA/DM-114/2022	4. N° DE PÁGINAS 101
5. TÍTULO E SUBTÍTULO: High-order conservative interpolation on overset meshes for unsteady aerodynamics applications			
6. AUTOR(ES): Renan Santos			
7. INSTITUIÇÃO(ÕES)/ÓRGÃO(S) INTERNO(S)/DIVISÃO(ÕES): Instituto Tecnológico de Aeronáutica - ITA			
8. PALAVRAS-CHAVE SUGERIDAS PELO AUTOR: Computational Fluid Dynamics; Unsteady aerodynamics; High-order methods; Overset grid.			
9. PALAVRAS-CHAVE RESULTANTES DE INDEXAÇÃO: Dinâmica dos fluidos computacional; Interpolação; Análise numérica; Mecânica dos fluidos; Equações de Euler-lagrange; Aerodinâmica; Física.			
10. APRESENTAÇÃO: <input checked="" type="checkbox"/> Nacional <input type="checkbox"/> Internacional			
ITA, São José dos Campos. Curso de Mestrado. Programa de Pós-Graduação em Ciências e Tecnologias Espaciais. Área de Sistemas Espaciais, Ensaios e Lançamentos. Orientador: Prof. Dr. João Luiz Filgueiras de Azevedo. Defesa em 08/08/2022. Publicada em 2022.			
11. RESUMO: The capability of handling unsteady flows over complex geometries with efficiency and high-order accuracy is quite often desirable for the aerospace industry. Recent research on high-order overset flux reconstruction methods have shown successful results over moving boundary problems without the need of remeshing. The ability of accurately handling such type of requirements is very important, for instance, when addressing rotary wing flows and similar problems. In the present study, a high-order flux reconstruction solver is implemented coupled with a high-order conservative interpolation approach and a kd-tree algorithm over the mesh nodes for data communication in the overset regions. The flow is modeled by the 2-D Euler equations discretized in space with a Spectral Differences method and an explicit strong stability-preserving Runge-Kutta scheme for time integration. In the overset grid scenarios, two unstructured grids are generated: a background mesh including all the fluid box domain and a near-body mesh. In order to determine which cell of the donor grid embeds a specific node in the receiver grid, both mesh nodes are implemented with a tree data structure expecting the logarithmic time complexity of O(k.logN) in the geometric search, where k is the number of flux points over the boundary interfaces of the receiver mesh and N the number of nodes in the donor grid. Furthermore, the solution is interpolated from the donor cell to the receiver grid point based on the donor cell polynomial expansion at the solution points and, then, imposed in a weak manner as a boundary condition to exactly reconstruct the flux with the approximate Riemann solver, as for any other interior face. The implementation is tested for different validation problems from the 5th International Workshop on High-Order CFD Methods (HiOCFD5). Additionally, accuracy and convergence studies are performed on both single and overset grid approaches and compared to results in the literature			
12. GRAU DE SIGILO: <input checked="" type="checkbox"/> OSTENSIVO <input type="checkbox"/> RESERVADO <input type="checkbox"/> SECRETO			